

Morpho-kinematics of the circumstellar envelope of the AGB star R Dor: a global view

P.T. Nhung¹*, D.T. Hoai¹†, P. Tuan-Anh¹, P. Darriulat¹, P.N. Diep¹, N.B. Ngoc¹, N.T. Phuong^{1,2} and T.T. Thai¹

¹*Department of Astrophysics, Vietnam National Space Center, Vietnam Academy of Science and Technology, 18, Hoang Quoc Viet, Nghia Do, Cau Giay, Ha Noi, Vietnam*

²*Korea Astronomy and Space Science Institute, 776 Daedeokdae-ro, Yuseong-gu, Daejeon 34055, Republic of Korea*

Accepted XXX. Received YYY; in original form ZZZ

ABSTRACT

We analyse new ALMA observations of the ^{29}SiO ($\nu=0, J=8-7$) and SO_2 ($\nu=0, 34_{3,31}-34_{2,32}$) line emissions of the circumstellar envelope (CSE) of the oxygen-rich AGB star R Dor. With a spatial resolution of ~ 2.3 au, they cover distances below ~ 30 au from the star providing a link between earlier observations and clarifying some open issues. The main conclusions are: 1) Rotation is confined below ~ 15 au from the star, with velocity reaching a maximum below 10 au and morphology showing no significant disc-like flattening. 2) In the south-eastern quadrant, a large Doppler velocity gas stream is studied in more detail than previously possible and its possible association with an evaporating planetary companion is questioned. 3) A crude evaluation of the respective contributions of rotation, expansion and turbulence to the morpho-kinematics is presented. Significant line broadening occurs below ~ 12 au from the star and causes the presence of high Doppler velocity components near the line of sight pointing to the centre of the star. 4) Strong absorption of the continuum emission of the stellar disc and its immediate dusty environment is observed to extend beyond the disc in the form of self-absorption. The presence of a cold SiO layer extending up to some 60 au from the star is shown to be the cause. 5) Line emissions from SO, ^{28}SiO , CO and HCN molecules are used to probe the CSE up to some 100 au from the star and reveal the presence of two broad back-to-back outflows, the morphology of which is studied in finer detail than in earlier work.

Key words: stars: AGB and post-AGB – circumstellar matter – stars: individual: R Dor – radio lines: stars.

1 INTRODUCTION

In the recent years, the availability of high sensitivity and high angular resolution observations, in particular from the Atacama Large Millimeter/submillimeter Array (ALMA), has shed new light on the mechanisms that govern the mass loss of evolved stars. At the same time it has revealed their complexity and many open questions are still awaiting an answer. Such is particularly the case of oxygen-rich AGB stars, for which the details of the formation of a dust-grain-driven wind are not fully understood. Recently, several such stars have been the object of detailed observations and studies; among these is R Dor, which is the subject of the present article.

R Dor, an oxygen-rich AGB star, is a semi-regular variable of the SRb type, belonging to spectral class M8IIIe, having an initial mass estimated between 1 and 1.5 M_{\odot} from the value of the $^{17}\text{O}/^{18}\text{O}$ ratio (Danilovich et al. 2017), a mass-loss rate of $\sim 1.6 \cdot 10^{-7} M_{\odot} \text{yr}^{-1}$ (Ramstedt & Olofsson 2014; Maercker et al. 2016) and a temperature of ~ 3000 K (Dumm & Schild 1998); it is close to the Sun, at a distance of only ~ 59 pc (Knapp et al. 2003); it displays no technetium in its spectrum (Lebzelter 1999) and has a $^{12}\text{CO}/^{13}\text{CO}$ abundance

ratio of ~ 10 (Ramstedt & Olofsson 2014). It has a dual period of 175 and 332 days (Bedding et al. 1998) and its infrared emission above black body between 1 and 40 μm wavelength shows an enhancement of aluminium oxide and melilite in the dust (Heras & Hony 2005).

Recent studies of the morpho-kinematics of the CSE of R Dor are summarized in Figure 1, which lists relevant references. The stellar disc and the stellar atmosphere that extends a very few au above it have been probed over a large range of wavelengths. Observations in the millimetre and sub-millimetre range are mostly from the Atacama Large Millimeter-sub-millimeter Array (ALMA) and use continuum or molecular lines emissions that probe preferentially the close neighbourhood of the star, such as the Λ doublet OH line (Vlemmings et al. 2019; Khouri et al. 2019). Evidence is found for short time variability (at month scale), hot spots covering a small fraction of the stellar disc, radial velocities at the 10 km s^{-1} scale, all revealing the impact of shocks associated with pulsations and convective cells. Similar results are obtained from observations in the optical and near-IR ranges, using the Very Large Telescope (VLT) equipped with SPHERE (Khouri et al. 2016). Large Doppler velocity wings are observed near the line of sight crossing the centre of the stellar disc, revealing the broad velocity dispersion in the inner layer (Decin et al. 2018; Hoai et al. 2020). In addition to the evidence for strong inhomogeneity and time variability, the stellar disc

* E-mail: pttnhung@vnsc.org.vn

† E-mail: dthoai@vnsc.org.vn

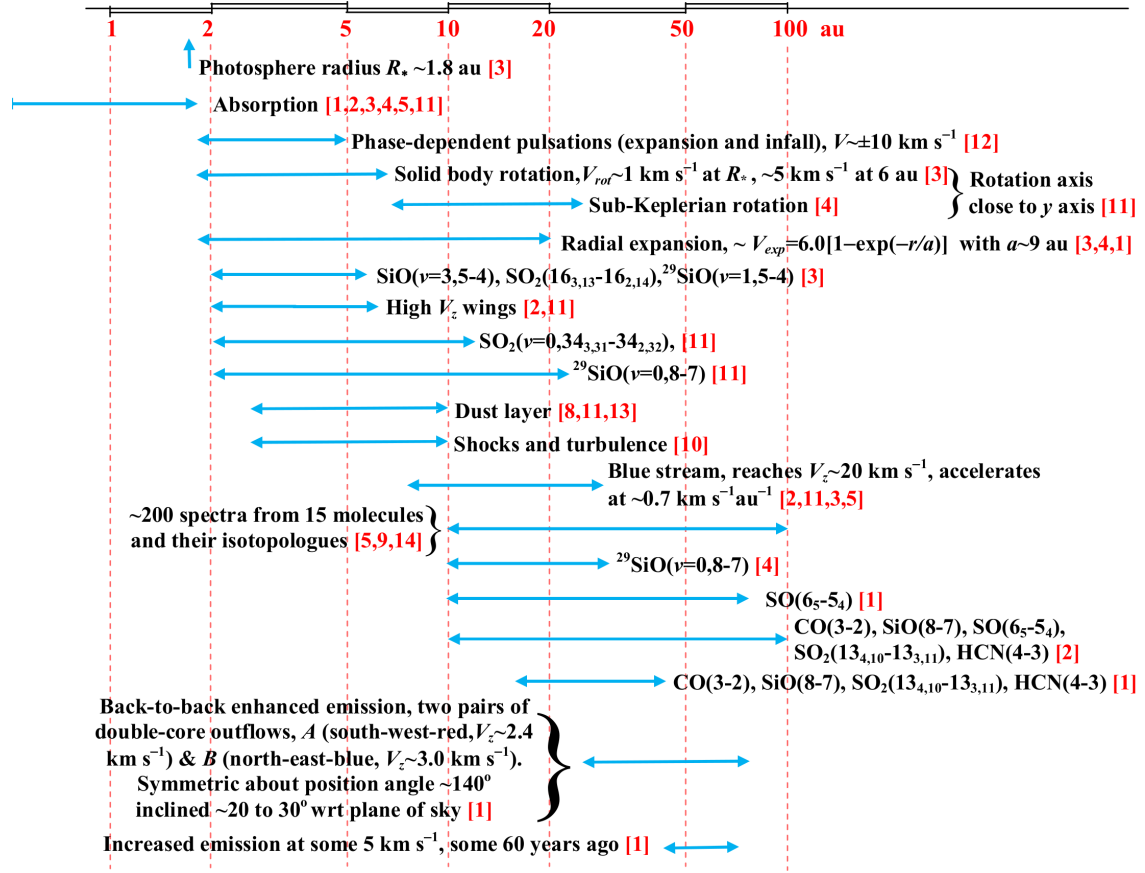


Figure 1. A summary of recently published articles on R Dor. Blue arrows indicate the radial range covered by each study. Red numbers in square brackets refer to the following articles: 1. Nhung et al. (2019) 2. Hoai et al. (2020) 3. Vlemmings et al. (2018) 4. Homan et al. (2018) 5. Decin et al. (2018) 6. Van de Sande et al. (2018) 7. De Beck & Olofsson (2018) 8. Khouri et al. (2016) 9. Danilovich et al. (2016) 10. Vlemmings et al. (2019) 11. This work. 12. Nowotny et al. (2010) 13. Decin et al. (2017) 14. Danilovich et al. (2020)

radius is measured at a 1.5 to 2 au scale dependent on wavelength; temperatures are estimated in the 2700 ± 300 K range.

Evidence for the presence of large dust grains, at 0.1 micron scale, within a very few au from the radiosphere is obtained from the study of continuum emission as well as from the observation of polarized light using SPHERE/ZIMPOL on the VLT (Khouri et al. 2016). Observations at infrared wavelengths using NACO on VLT (Norris et al. 2012) give similar results. This suggests a scenario where the wind is driven by photon scattering on large transparent grains very close to the star, rather than by radiation pressure on silicate grains, which is too small to drive the winds of O-rich AGB stars (Woitke 2006). Numerous multi-wavelength studies, using in particular Herschel and ALMA observations, have addressed the question of the composition of the dust and of the nature of its main precursors, generally concluding that aluminium bearing molecules play a dominant role (Heras & Hony 2005; Decin et al. 2018). Decin et al. (2017) study the line profiles of AlO, AlOH and AlCl and suggest the presence of large gas-phase $(\text{Al}_2\text{O}_3)_n$ clusters ($n > 34$) close to the star. Moreover, Takigawa et al. (2019) have shown that transition alumina containing ~10% of Si rather than amorphous alumina with pure Al_2O_3 composition is the most plausible source of the dust emission from alumina-rich AGB stars (see also Karovicova et al. 2013). Analyses of molecular line profiles from single dish observations provide a host of useful information on the gas and dust composition of the CSE up to

a few 100 au from the star, an important result being the confinement of SiO to shorter distances than CO, interpreted in part as the result of a progressive condensation of SiO gas molecules onto dust grains (Schöier et al. 2004). De Beck & Olofsson (2018) and Decin et al. (2018) perform extensive spectral scans of the envelope, the latter detecting gaseous precursors of dust grains such as SiO, AlO, AlOH, TiO, and TiO_2 . Danilovich et al. (2016, 2017, 2019, 2020) study sulphur-bearing and water molecules and HCN abundances are measured by Schöier et al. (2013) and by Van de Sande et al. (2018).

Significant rotation of the inner CSE has been detected by Homan et al. (2018) and Vlemmings et al. (2018). The former authors use ALMA observations of the $^{28}\text{SiO}(v=1, J=8-7)$ line emission to probe the ~6 to ~25 au radial range with an angular resolution of ~9 au. Their data are well described by a nearly edge-on disc in sub-Keplerian rotation, with a projected rotation velocity of ~6 km s^{-1} at a distance of 12 au. The latter authors use ALMA observations of the $\text{SiO}(v=3, J=5-4)$ and $\text{SO}_2(J_{K_a, K_c}=16_{3,13}-16_{2,14})$ line emissions with an angular resolution of ~2 au to probe the inner layer from the radiosphere up to some 15 au. Their data give no evidence for disc morphology and are well described by solid-body rotation, again with a projection rotation velocity of ~6 km s^{-1} at a distance of 12 au. The difference between the two models is largely the result of the different radial ranges probed by the observations. Both authors argue that the presence of significant rotation is most easily

Table 1. Parameters of the ^{29}SiO and SO_2 emission lines. E_u is the energy of the upper level of the transition. The frequency f corresponds to a wavelength $\lambda = 0.875$ mm and a transition temperature of 16.5 K.

Molecule	Transition	f (GHz)	E_u (K)
^{29}SiO	$\nu=0, J=8-7$	342.98084800	74.08
SO_2	$\nu=0, 34_{3,31}-34_{2,32}$	342.76162320	581.92

explained by the transfer of angular momentum from a companion to the star. The presence of a blue-shifted feature in the south-eastern quadrant, extending to some 25 au in projected distance from the star and reaching near 20 km s^{-1} in Doppler velocity (Decin et al. 2018; Vlemmings et al. 2018; Hoai et al. 2020) is invoked as suggesting its association with such companion.

Finally, a detailed study of the outer region of the CSE, beyond some 25 au, shows the presence of outflows and of cavities suggesting a complex history of mass ejection (Nhing et al. 2019, hereafter referred to as Paper I).

The present work studies the emissions of two molecular lines that have been observed by ALMA: ^{29}SiO ($\nu=0, J=8-7$) and SO_2 ($\nu=0, 34_{3,31}-34_{2,32}$), thereafter simply referred to as ^{29}SiO and SO_2 . Parameters of relevance are listed in Table 1.

The paper is organized as follows: after a description of observations and data reduction, we present in Section 3 a general picture of the morpho-kinematics of the CSE as obtained from the new results discussed in the present work and taking into account analyses published earlier. Section 4 discusses some properties of the inner layer, accounting for absorption and including rotation, expansion and contributions to the line width. Section 5 addresses questions related to the observed properties of the south-eastern blue-shifted feature. Section 6 explores the CSE to larger distances from the star using other molecular line emissions as probes with the aim of explaining what causes the strong absorption of the SiO lines. A last section summarizes the main results and concludes.

2 OBSERVATIONS AND DATA REDUCTION

The data are retrieved from ALMA archives, project 2017.1.00191.S, observed in November 2017 in band 7 with antennas in the C43-9 configuration. The observations were made in two blocks using 44 and respectively 45 antennas. The total time on source was 90 min, 45 min for each block. Visibilities are averaged over 20 s wide time intervals. Baselines span between 100 m and 12 km (Figure 2) and the maximal recoverable scale, evaluated for a wavelength of 0.87 mm and an effective minimal baseline of 300 m, is 0.36 arcsec. We select a frequency interval of 81 channels corresponding to a Doppler velocity interval of 69 km s^{-1} , each Doppler velocity bin being 0.854 km s^{-1} wide. The systemic velocity of R Dor (7 km s^{-1}) is taken as origin. The data were reduced using standard scripts for continuum emission and two line emissions: ^{29}SiO ($\nu=0, J=8-7$) and SO_2 ($34_{3,31}-34_{2,32}$).

We calibrated the data using the scripts provided by the ALMA staff. Deconvolution and cleaning were done with natural weighting using two different codes: CASA¹ and GILDAS². The line data were processed without continuum subtraction. The beams obtained with CASA and GILDAS (FWHM) were $34 \times 25 \text{ mas}^2$ and $41 \times 35 \text{ mas}^2$ respectively. In both cases we use pixels of $5 \times 5 \text{ mas}^2$. We found that the differences between the results obtained with the two codes are

simply explained by the differences in beam size and have negligible impact on the results of our analyses. In what follows we use the GILDAS results as default but we checked their consistency with the CASA results whenever possibly relevant. Brightness distributions (Figure 2) show a noise level (1σ) of $1.4 \text{ mJy beam}^{-1}$ for ^{29}SiO and $1.1 \text{ mJy beam}^{-1}$ for SO_2 . Additional information is provided in Section 6.1. Channel maps are shown in the Appendix (Figures A1 and A2).

Moreover, in Section 6, we use observations of other molecular lines that have been briefly considered in Paper I: $^{28}\text{SiO}(8-7)$, $\text{CO}(3-2)$ and $\text{HCN}(4-3)$. Their emission was detected with a similar beam size but in less favourable observational conditions than for the $\text{SO}(J_K=6_5-5_4)$ line, which was the central subject of Paper I (see Section 6.2). They are from project 2013.1.00166.S observed in summer 2015 in band 7 with an average of 35 antennas in the C34-7 configuration. They include two independent sets of ^{28}SiO data, hereafter referred to as $^{28}\text{SiO I}$ and $^{28}\text{SiO II}$. Paper I used data reduced by the ALMA staff with continuum subtraction in the uv plane. As the uv coverage for short baselines is poor, we reduced these data anew, using GILDAS with natural weighting and without continuum subtraction. A summary of the main parameters and results is listed in Table 2 and illustrated in Figure 3, which shows the baseline and brightness distributions obtained in each case. We paid much attention to the impact of the short spacing problem on the quality and reliability of the reduced data. This is illustrated in Figure 3b: the $^{28}\text{SiO I}$ and $^{28}\text{SiO II}$ sets, although having similar baseline distributions, display very different visibility distributions. The simple addition of a few short baselines is the cause. Accordingly, we restrict the analysis to distances from the star not exceeding 60 au (1 arcsec). Moreover, we disregard the $^{28}\text{SiO I}$ set of data as not adding significant information to that obtained from the $^{28}\text{SiO II}$ set.

We use orthonormal coordinates with the x axis pointing east, the y axis pointing north and the z axis pointing away from Earth. Position angles, ω , are measured counter-clockwise from north.

3 OVERALL PICTURE OF THE CSE

Figure 4 displays the sky maps of the integrated intensity (moment 0) and mean Doppler velocity $\langle V_z \rangle$ (moment 1) for both the ^{29}SiO and SO_2 lines. While ^{29}SiO emission is seen to extend up to some 40 au projected distance from the star, SO_2 emission is limited to some 12 au. The high excitation energy of the SO_2 line prevents it from populating the outer CSE as the temperature can be expected to take a value of $\sim 1100 \text{ K}$ at 6 au from the star and to decrease as $r^{-0.65}$ (Decin et al. 2018; Homan et al. 2018; Van de Sande et al. 2018). The south-eastern blue stream stands out in the ^{29}SiO map, more clearly than in previous publications, both because of the better match with the radial range being probed and the better sensitivity and angular resolution. For both lines the north-western half of the $\langle V_z \rangle$ map is red-shifted, the south-eastern half blue-shifted and the inner layer of the CSE gives evidence for rotation about an axis projecting close to north.

3.1 The inner layer

Figures 5 to 8 illustrate the main properties of the inner CSE layer, which we present in a set of rings surrounding the star, each 0.05 arcsec (3 au) wide and covering $0.05 < R < 0.20$ arcsec as illustrated in Figure 5. The stellar disc, known to have a radius of ~ 1.8 au (0.03 arcsec) at mm wavelength (Vlemmings et al. 2018), is here

¹ <http://casa.nrao.edu>

² <https://www.iram.fr/IRAMFR/GILDAS>

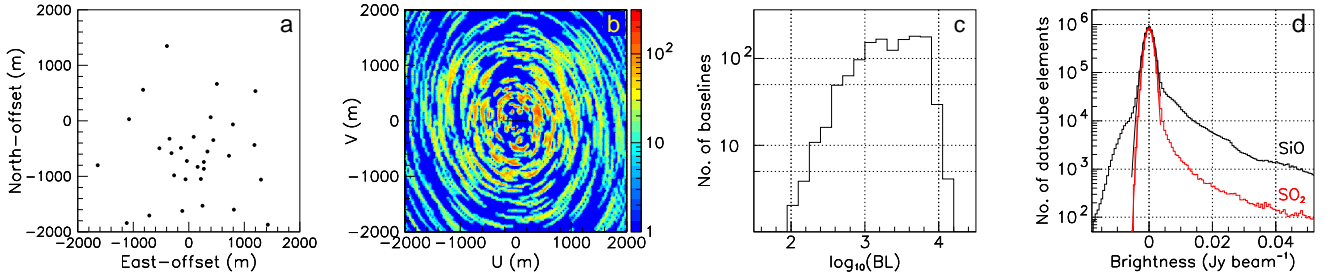


Figure 2. The antenna configuration (a) and uv coverage (b) are shown for the central region ($|u|$ and $|v| < 2000$ m). The colour scale in panel b shows the density of visibility measurements (in 40×40 m² bin) (c): distribution of the baselines; the abscissa is $\log_{10}(\text{BL})$, the decimal logarithm of the baseline length measured in meters. (d): brightness distributions for ^{29}SiO (black) and SO_2 (red) in a $R < 1$ arcsec circle.

Table 2. ^{28}SiO , CO, HCN and SO observations. f is the frequency, MRS the maximal recoverable scale, N the number of antennas.

Line	f (GHz)	Beam (mas ²)	MRS (au)	N	Noise (mJy beam ⁻¹)	Date	Time on source
^{28}SiO II	347.3	220 \times 170	80	38	18	Aug 2015	21 mn
CO	345.8	180 \times 140	80	32	14	Sep 2015	21 mn
HCN	354.5	157 \times 145	78	34	8	Aug 2015	26 mn
SO	251.8	154 \times 147	136	45	1.2	Dec 2017	2.7 hr

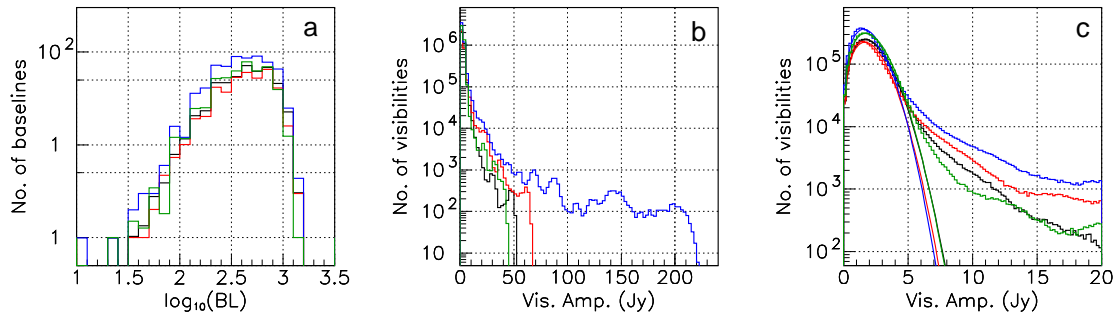


Figure 3. Observation and reduction of the ^{28}SiO I (red), ^{28}SiO II (blue), CO (black) and HCN (green) data. (a): dependence of the number of baselines on the decimal logarithm of the baseline lengths measured in meters, $\log_{10}(\text{BL})$. (b): distribution of the visibility amplitude $|U|$ in the interval $|V_z| < 7$ km s⁻¹. (c): zoom of panel b showing noise fits of the form $|U|\exp(-1/2|U|^2/\sigma^2)$. They give $\sigma=1.6, 1.5, 1.7$ and 1.7 Jy for ^{28}SiO I, ^{28}SiO II, CO and HCN respectively.

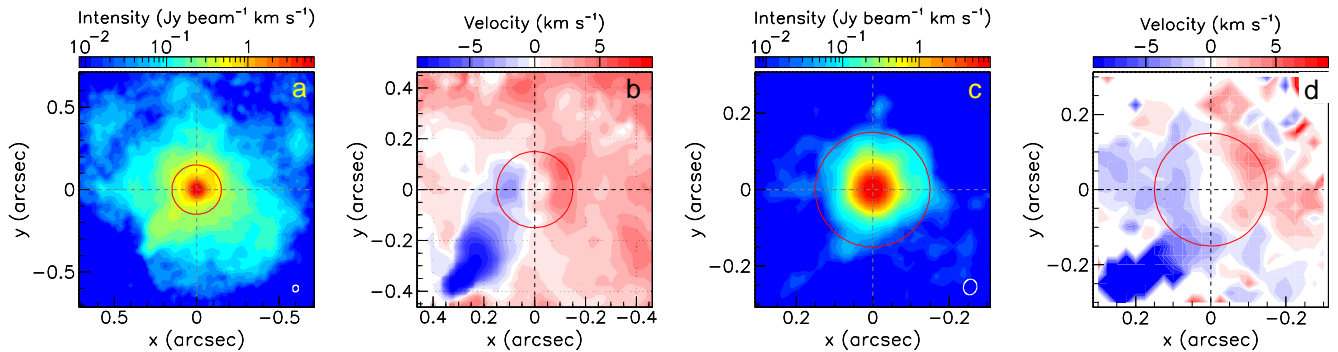


Figure 4. Maps of the intensity (a,c) and of $\langle V_z \rangle$ (b,d), respectively integrated and averaged over $|V_z| < 24$ km s⁻¹ for ^{29}SiO (a,b) and SO_2 (c,d) emissions. Note the different scales. In both cases a 3σ cut has been applied. In the $\text{SO}_2 \langle V_z \rangle$ map the colour scale is saturated over the south eastern blue stream where the intensity is near noise level. The red circle ($R < 9$ au = 0.15 arcsec) shows the inner region dominated by rotation.

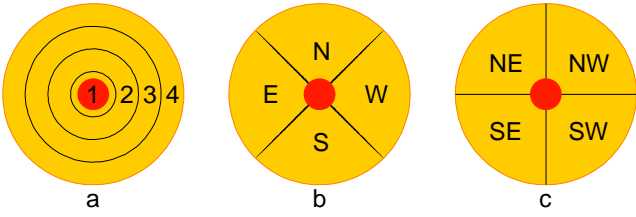


Figure 5. Numbering of the rings (a) and quadrants (b,c). The red circle shows the star with a radius of 0.035 arcsec = 2.1 au; the yellow circle has a radius of 12 au = 0.2 arcsec; each ring is 3 au = 0.05 arcsec wide.

represented with a radius of 0.035 arcsec. Figure 6 displays the Doppler velocity spectra integrated over it for both ^{29}SiO and SO_2 emissions. They are mostly seen in absorption. The ^{29}SiO spectrum shows a clear absorption peak occurring in the outer layer where the slow wind has reached a velocity of ~ 4 km s $^{-1}$. In addition, it also displays absorption by the inner layer, revealing a Doppler velocity distribution extending up to $|V_z| \sim 20$ km s $^{-1}$. Its precise shape is not expected to be significantly affected by rotation but to tell about the radial increase of the expansion velocity as well as about line width; the latter are expected to receive important contributions from shocks associated with pulsations and convective cell ejections (Freytag et al. 2017, and references therein). The red side of the inner layer is seen in emission, the line width of the outer layer being too small to significantly populate Doppler velocities exceeding ~ 10 km s $^{-1}$, ~ 15 km s $^{-1}$ above the mean Doppler velocity at such a distance from the star.

The SO_2 spectrum is also mostly seen in absorption, displaying a shape qualitatively similar to that of the ^{29}SiO spectrum, with a narrow absorption peak near -4 km s $^{-1}$. However, the scale is very different, both in flux density and in Doppler velocity. The amplitude of the absorption peak is only 18% of the continuum level instead of being total for ^{29}SiO and the part of the spectrum seen in emission is centred at ~ 6 km s $^{-1}$ instead of ~ 13 km s $^{-1}$. A reliable interpretation of the features displayed in Figure 6 requires accounting, at least approximately, for optical thickness, which we do in Section 4.

Figures 7 and 8 display the Doppler velocity spectra averaged in the rings and quadrants defined in Figure 5 and covering projected distances from the star between 0.05 and 0.20 arcsec (3 and 12 au). While the ^{29}SiO spectra show strong absorption by the outer CSE layer, seen as a peak at ~ -4 km s $^{-1}$, the SO_2 spectra are approximately Gaussian and display no absorption feature. Good fits to both ^{29}SiO and SO_2 spectra are accordingly obtained using the simple form

$$I = I^* + I_0 G(V_z, V_{z0}, \sigma_0) - A G(V_z, -4.0, 1.2)$$

where $G(V_z, a, b) = \exp(-1/2[V_z - a]^2/b^2)$.

The first term, I^* , accounts for a small continuum contribution, particularly significant in the inner ring; I_0 , V_{z0} and σ_0 define the Gaussian emission and the last term accounts for the absorption by the outer layer. A is set to zero in the SO_2 case and is such that the absorption is total at $V_z = -4.0$ km s $^{-1}$ in the ^{29}SiO case, namely $A = I^* + I_0 G(V_z, -4.0, 1.2)$; the width of the absorption term is fixed with a σ of 1.2 km s $^{-1}$.

Tables A1 and A2 of the Appendix list the values of the best-fit parameters. For both lines the values of I^* show a same excess of N and NW over S and SE by a factor 2 in the innermost ring, reflecting a small asymmetry of continuum emission.

If the density of the gas in rotation had a significantly flattened distribution along the equator, in the form of a nearly edge-on disc as

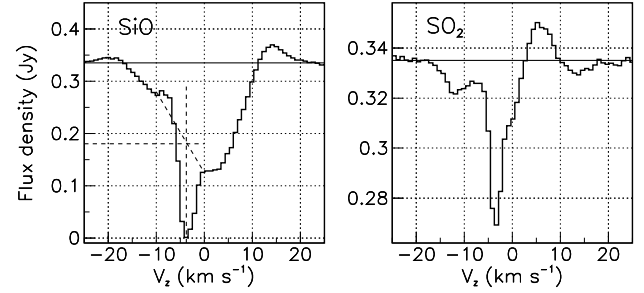


Figure 6. Doppler velocity spectra integrated over the stellar disc ($R < 0.035$ arcsec, region 1 of Figure 5) for ^{29}SiO (left) and SO_2 (right, note the zero-suppressed scale of ordinate). The dashed lines in the left panel illustrate how we estimate I_{mid} in Section 3.2.

Table 3. Parameters of the sine wave fits of the form $A + B \sin(\omega - \omega_0)$ to the mean Doppler velocity distributions displayed in Figure 9. A cut of 3σ has been applied to the data; the intensity is integrated and the Doppler velocity averaged over the $|V_z| < 12$ km s $^{-1}$ interval.

Line	R range (mas)	Mean Doppler velocity		
		A	B	ω_0 ($^\circ$)
^{29}SiO	50-100	0.6	2.7	179
	100-150	1.0	3.8	191
	150-200	1.0	3.0	196
SO_2	50-100	-0.2	1.8	177
	100-150	-0.1	3.2	200
	150-200	-0.6	2.8	215

suggested by Homan et al. (2018), the intensity projected on the sky plane should display significant ellipticity: its distribution in each ring as a function of position angle ω should take the form of a $1 - \zeta \cos(2\omega)$ term with ζ providing a measure of the flattening and the distribution reaching its two maxima near the E and W directions and its two minima near the S and N directions. Figure 9a,b displays these distributions; there is no evidence for such a quadrupolar term but instead dipole sine waves, of the form $A + B \sin(\omega - \omega_0)$ are seen to give reasonable fits. They reach their maxima in the NW direction with $\omega_0 \sim 330^\circ$ and the amplitudes of the oscillation are $\sim 20\%$ of the average emission level. The absence of a quadrupolar term sheds doubts on the previously suggested evidence for the presence of an edge-on disc. Figure 9c,d displays the distributions of the mean Doppler velocity; sine waves, as expected for rotation, are seen to give good fits (Table 3). They reach their maxima in the W direction with $\omega_0 \sim 190^\circ$ and the amplitude of the oscillations reaches ~ 4 km s $^{-1}$. From the east-west asymmetry displayed by the values of V_{z0} , one can see that the rotation reaches a maximal velocity within the displayed range of R , namely below 0.15 arcsec (9 au); beyond the outer ring the blue stream starts contributing significantly to the mean Doppler velocity. A detailed discussion of these observations is presented in Section 4. A clear enhancement of the line width is seen in the inner ring for both ^{29}SiO and SO_2 .

Figure 10 displays the dependence on position angle of the ^{29}SiO intensity and mean Doppler velocity in successive rings, each 0.04 arcsec (2.4 au) wide. It complements the channel maps displayed in the Appendix and covers not only the inner layer, with the confinement of rotation to projected distances from the star not exceeding 15 au, but also larger distances studied in the following sections, with the appearance of the blue stream at $R \sim 0.2$ arcsec (12 au) and of the

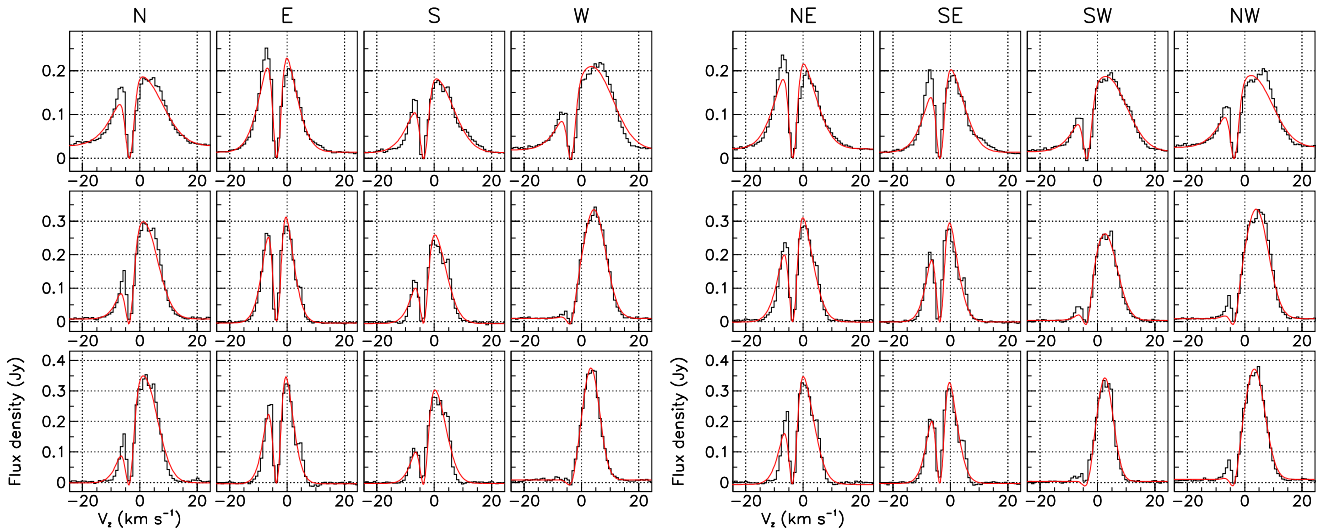


Figure 7. Doppler velocity spectra (black) of ^{29}SiO emission. From left to right: quadrants N, E, S, W, NE, SE, SW and NW (see Figure 5). From up down: rings 2, 3 and 4. The fits (red) are described in the text and their parameters listed in Table A1.

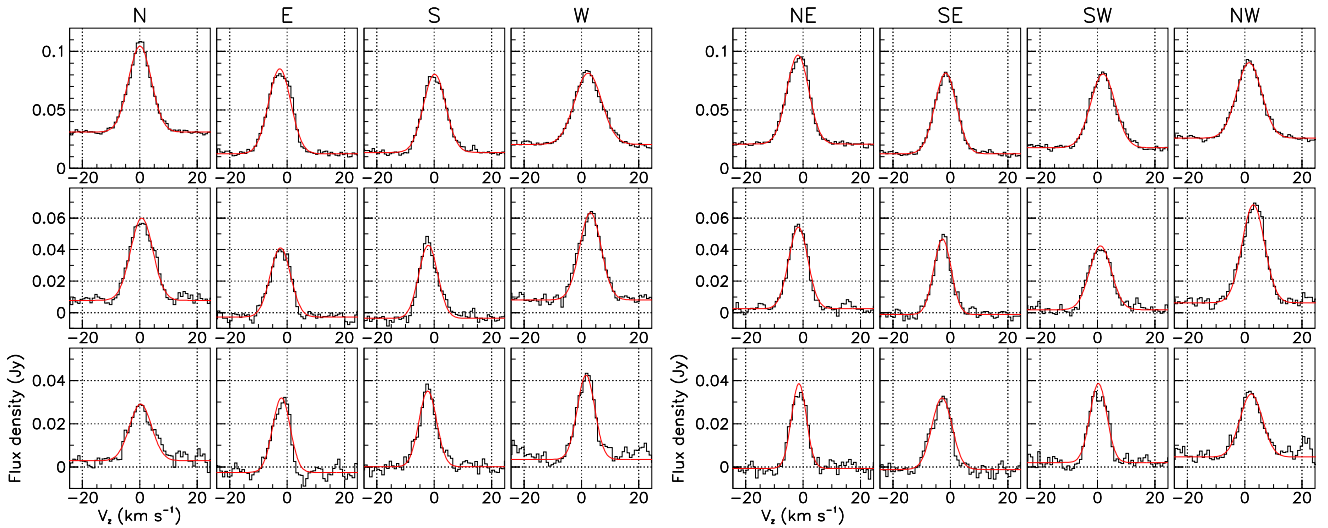


Figure 8. Doppler velocity spectra (black) of SO_2 emission. From left to right: quadrants N, E, S, W, NE, SE, SW and NW (see Figure 5). From up down: rings 2, 3 and 4. The fits (red) are described in the text and their parameters listed in Table A2.

south-western outflow identified earlier in Paper I at $R \sim 0.45$ arcsec (27 au).

3.2 Absorption over the stellar disc

In the preceding section (Figure 6 left), we noted the presence of a nearly total absorption peak at ~ -4 km s $^{-1}$ in the ^{29}SiO data, extending to large values of R as clearly illustrated in Figure 11: the absorption is seen to extend well beyond $R \sim 15$ au, far from the stellar disc (panels a and b). This is also clearly apparent on the channel maps (Figure A1). Comparison between the brightness distributions measured in the $V_z = -4$ km s $^{-1}$ and $V_z = +4$ km s $^{-1}$ Doppler velocity channels shows that indeed the former detects only very little signal above noise (panels c and d). Both features, the nearly total absorption over the stellar disc and its extension beyond it, are surprising. We discuss the former below but postpone a discussion of the latter to

Section 6 because it requires analyses of line emissions that explore larger distances from the star, up to 100 au or so.

Quantitatively, we can safely place a $3\text{-}\sigma$ upper limit of 4.2 mJy beam $^{-1}$ (10 mJy over the stellar disc) on the brightness measured at maximal absorption, $V_z \sim -4$ km s $^{-1}$, over the stellar disc ($R < 0.035$ arcsec). While local thermal equilibrium (LTE) is not expected to provide a reliable description of the CSE, in particular in the close neighbourhood of the star, its prediction provides a useful reference with which to compare observations. For a given velocity V_z and a brightness I_0 [Jy arcsec $^{-2}$] on the entrance side of a slab of thickness dz [arcsec], density n [molecules cm $^{-3}$] and temperature T [K], the brightness I [Jy arcsec $^{-2}$] at the exit side is simply the sum $I = I_0 + \varepsilon$, where ε is the emission of the slab, when absorption is neglected. The effect of absorption, described by the optical depth τ , is to have instead

$$I = I_0 e^{-\tau} + \varepsilon(1 - e^{-\tau})/\tau = \varepsilon/\tau + (I_0 - \varepsilon/\tau)e^{-\tau} \quad (1)$$

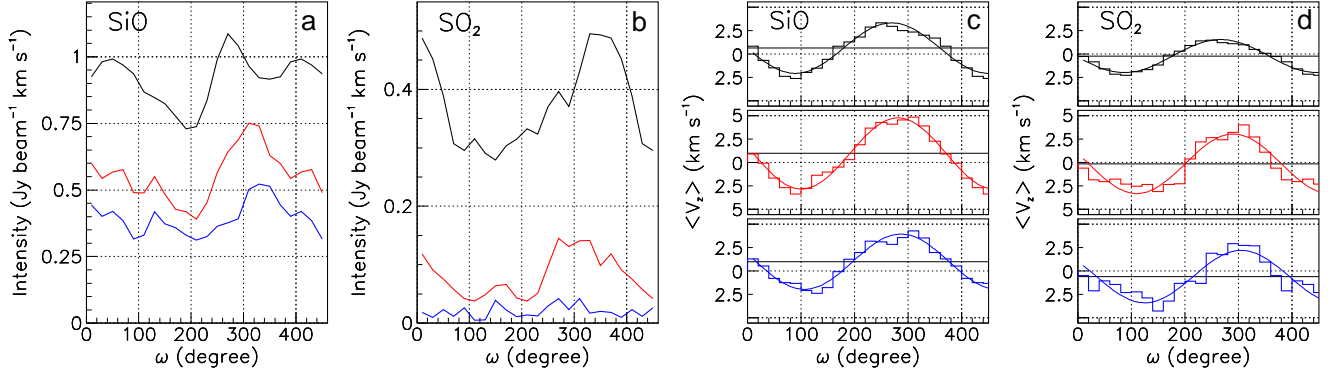


Figure 9. Dependence on position angle of the intensity (a,b) and mean Doppler velocity (c,d) averaged over rings 2 (black), 3 (red) and 4 (blue) for ^{29}SiO (a,c) and SO_2 (b,d). The intensity is integrated and the velocity averaged over the interval $|V_z| < 12 \text{ km s}^{-1}$.

where ε is given by Relation 2 below:

$$\begin{aligned} \varepsilon &= hf / (4\pi\Delta f) n A_{ji} f_{\text{pop}} dz \\ &= 0.33 \cdot 10^6 N A_{ji} f_{\text{pop}} / \Delta V, \quad f_{\text{pop}} = (2J+1) e^{-E_u/T} / T \end{aligned} \quad (2)$$

with J and E_u being the angular momentum quantum number and energy of the upper level, N the column density in molecules $\text{cm}^{-3} \text{ arcsec}$, A_{ji} the Einstein coefficient, ΔV the FWHM of the profile measured in km s^{-1}

and where τ is given by Relation 3 below:

$$\begin{aligned} \tau &= c^2 / (8\pi f^2 \Delta f) (e^{\Delta E/T} - 1) n A_{ji} f_{\text{pop}} dz \\ &= 2.9 \cdot 10^7 \varepsilon (e^{\Delta E/T} - 1) / f^3 \quad (f = 343 \text{ GHz}) \end{aligned} \quad (3)$$

When the column density $N = n \times dz$ increases, I varies from I_0 to ε/τ . In case of absorption, $I_0 > \varepsilon/\tau$, I is always larger than ε/τ , a lower limit to the emission of an optically thick shell. In the present case, where the energy of the transition, $\Delta E = 16.4 \text{ K}$, can be expected to be much smaller than the temperature T , we can approximate ε/τ [Jy arcsec^{-2}] = T [K] / 11.8. Integrating over the beam area, $\sim 1.6 \cdot 10^{-3} \text{ arcsec}^2$, we obtain a lower limit for the brightness of $1.6T/11.8 \text{ mJy beam}^{-1}$ to be compared with the $3\text{-}\sigma$ limit of $4.2 \text{ mJy beam}^{-1}$, meaning an upper limit of $11.8 \times 4.2 / 1.6 \sim 30 \text{ K}$ on T . Such a low value seems unlikely at such short distance from the star. The assumptions made are very crude but the fact remains that however large absorption may be, the outer part of the layer cannot be prevented from shining. This result is independent from the value of ε , namely of the column density. We note that in the case of Mira A (Wong et al. 2016) the brightness measured at maximal absorption exceeds 20% of the continuum level, compared with $< 3\%$ in the present case.

The above argument applies in particular to the outer layer, which is expected to host less turbulence, shocks and condensing dust than the inner layer does and where Doppler velocities can be assumed to stay within the interval $-10 < V_z < 0 \text{ km s}^{-1}$. Such assumption implies that the absorption observed outside this interval is confined to the inner layer. We accordingly define three values of the flux density over the stellar disc at $V_z \sim -4 \text{ km s}^{-1}$: inflowing, $I_{\text{in}} \sim 0.34 \text{ Jy}$, intermediate, $I_{\text{mid}} \sim 0.17 \text{ Jy}$ measured as the mean between the values of the brightness measured at $V_z = -10 \text{ km s}^{-1}$ and $V_z = 0$ (see Figure 6-left) and outflowing, $I_{\text{out}} < 0.01 \text{ Jy}$. At $V_z \sim -4 \text{ km s}^{-1}$ the flux density over the stellar disc decreases therefore from 0.34 Jy near the star to 0.17 Jy outside the inner layer and $< 0.01 \text{ Jy}$ outside the outer layer.

We first calculate ε and τ at a temperature $T \sim 270 \text{ K}$ using Relations 2 and 3 for ^{29}SiO . We use a column density N [molecules

$\text{cm}^{-3} \text{ arcsec}] = 0.7$ obtained by integration from $r = 0.8$ to 1.0 arcsec for a $^{28}\text{SiO}/\text{H}_2$ abundance of $5.5 \cdot 10^{-5}$ (Van de Sande et al. 2018), an isotopic ratio $^{29}\text{Si}/^{28}\text{Si} = 8\%$ (De Beck & Olofsson 2018) and an H_2 density of the form $1.6 \cdot 10^7 (r/0.2)^{-2}$ [molecules cm^{-3}], meaning a mass-loss rate of $\sim 1.6 \cdot 10^{-7} M_{\odot} \text{ yr}^{-1}$. Writing $J = 8$, $E_u = 74 \text{ K}$, $A_{ji} = 2.1 \cdot 10^{-3} \text{ s}^{-1}$, we obtain $\varepsilon = 8.2 \cdot 10^3 e^{-74/T} / (T \Delta V)$ and $\tau = 9.7 \cdot 10^4 e^{-74/T} / (T^2 \Delta V)$. Namely, at $T = 270 \text{ K}$, $\varepsilon = 8.2 \text{ Jy arcsec}^{-2}$ and $\tau = 0.36$ for $\Delta V = 2.8 \text{ km s}^{-1}$: the self-absorbed emission is $\sim 27 \text{ mJy}$ over the stellar disc, nearly 3 times the upper limit placed on the observed emission. Repeating the same calculation for $0.2 < r < 0.4 \text{ arcsec}$ gives $\varepsilon = 46 \text{ Jy arcsec}^{-2}$ and $\tau = 1.0$, respectively, the self-absorbed emission being $\sim 117 \text{ mJy}$ over the stellar disc. For the whole range, $0.2 < r < 1 \text{ arcsec}$, and $I_{\text{mid}} = 0.17 \text{ Jy}$ we find $I_{\text{out}} = 152 \text{ mJy}$ over the stellar disc, over an order of magnitude above the observed upper limit of 10 mJy .

We can repeat the above argument in the case of SO_2 emission. The abundance relative to H_2 is now of the form $5 \cdot 10^{-6} \exp[-(r/1.78)^2]$ (Danilovich et al. 2016, 2020), $E_u = 581.92 \text{ K}$ and $A_{ji} = 3.45 \cdot 10^{-4} \text{ s}^{-1}$, but the relation $\tau \sim 11.8 \varepsilon / T$ still applies. We estimate $I_{\text{mid}} = 0.325 \text{ Jy}$ and $I_{\text{out}} = 0.27 \text{ Jy}$. For the whole range, $0.2 < r < 1 \text{ arcsec}$, we find $I_{\text{out}} = 0.32 \text{ Jy}$.

In summary, for ^{29}SiO , below $\sim 12 \text{ au}$ and at $V_z \sim -4 \text{ km s}^{-1}$, the inner layer absorbs $\sim 40\%$ of the continuum emission ($\sim 60\%$ at $V_z = 0$) and is expected to host shocks and turbulence. We study it in Section 4. For SO_2 , at $V_z \sim -4 \text{ km s}^{-1}$, the inner layer absorbs only 2% of the continuum emission and the outer layer absorbs 17% of the inner layer emission. Beyond $\sim 12 \text{ au}$ and at $V_z \sim -4 \text{ km s}^{-1}$, we detect no emission for ^{29}SiO , implying that the outer layer not only absorbs completely the emission of the inner layer but also its own emission, which we discuss in Section 6. We have shown that a simple LTE model cannot produce such a result if the temperature takes values as expected in the literature and predicts an emission an order of magnitude larger than observed. This result suggests that such absorption is more likely to happen at large radii, say above 40 au , where the temperature is expected to be closer to 200 K (Van de Sande et al. 2018) and where an enhancement of emission has been observed (Paper I). This is further discussed in Section 6.

3.3 The blue stream

The blue stream is seen clearly on the channel maps of both ^{29}SiO and SO_2 emissions. It covers projected distances from the star reaching $\sim 30 \text{ au}$ for the former (Figure A1) and $\sim 20 \text{ au}$ for the latter (Figure

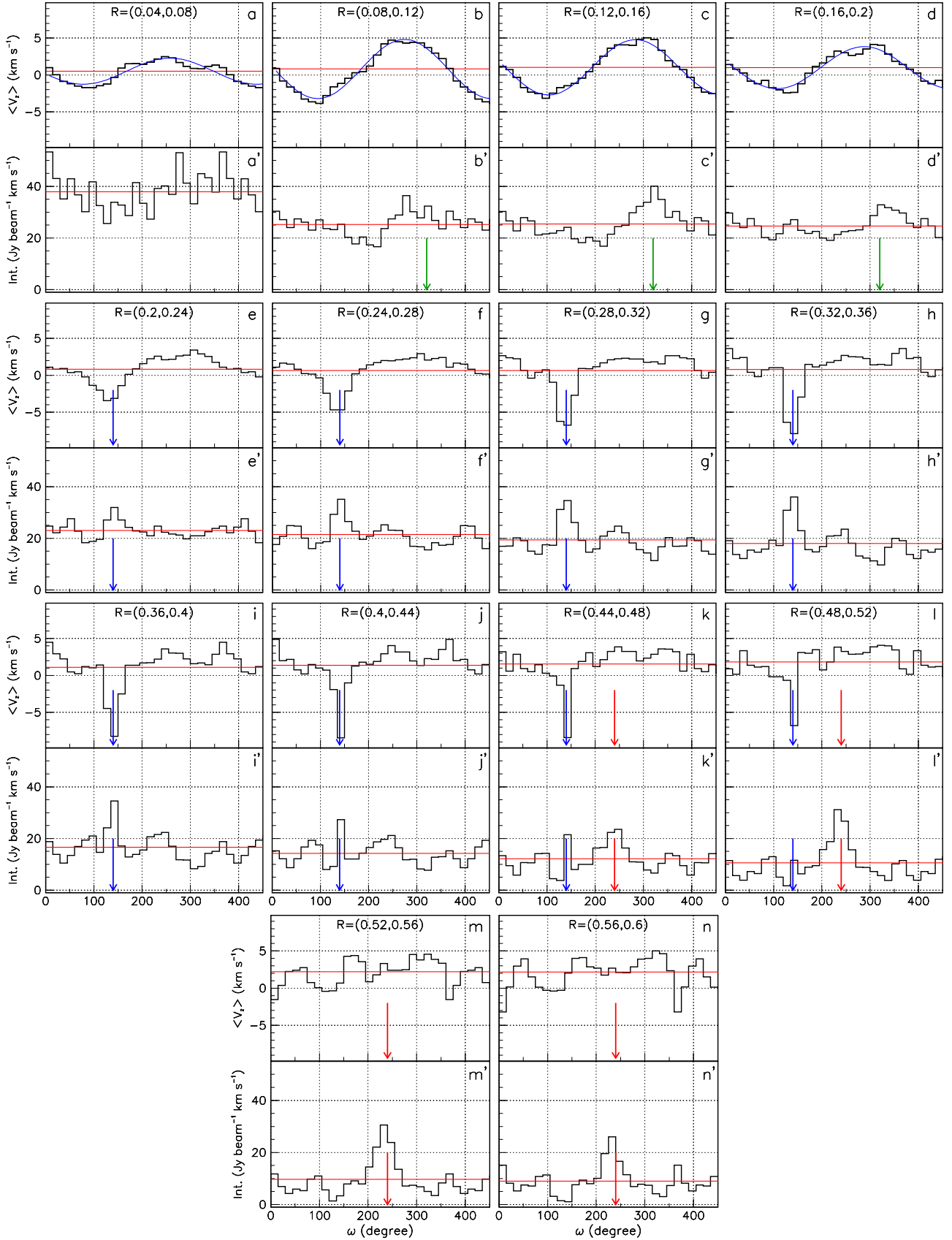


Figure 10. ^{29}SiO emission. Dependence on position angle of the mean Doppler velocity (a to n) and of the intensity (a' to n') in successive rings (as labelled above each velocity panel). The red line shows the mean value, the blue arrow is at 140° , the green arrow at 320° and the red arrow at 240° . The blue lines are sine wave fits.

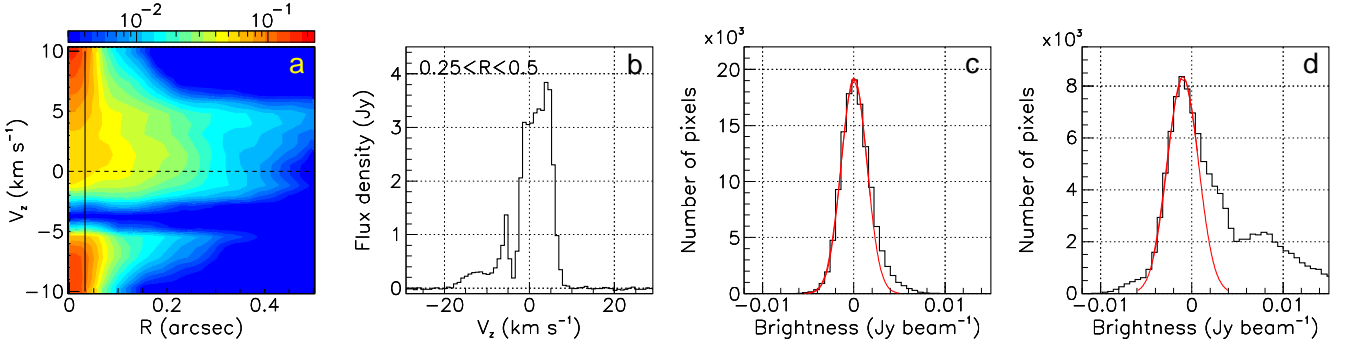


Figure 11. Absorption of the ^{29}SiO emission. (a): PV map showing the brightness (in Jy beam^{-1}) averaged over position angle as a function of Doppler velocity, V_z , vs projected distance from the star, R . The vertical line shows the size of the stellar disc. (b): Doppler velocity spectrum integrated in the ring $0.25 < R < 0.5$ arcsec. (c) and (d): brightness distributions integrated over $R < 1$ arcsec in the $V_z = -4 \text{ km s}^{-1}$ (c) and $V_z = +4 \text{ km s}^{-1}$ (d) frequency channels.

A2) at a mean position angle of $\sim 140^\circ$. In order to define it precisely we measure for each line its position in each frequency interval separately and fit straight lines through the points. Figure 12 displays intensity maps integrated over relevant Doppler velocity intervals. Panel c shows the dependence of the stream Doppler velocity on R defined as described above, for each frequency interval separately. To a good approximation it displays a constant projected acceleration of $39.2 \pm 0.5 \text{ km s}^{-1} \text{ arcsec}^{-1}$. A priori, there is no reason for such projected linearity: it may be destroyed by de-projection and, even if it were not, it would require that the force driving the wind is approximately the sum of a constant term and an r^{-2} term, the latter compensating gravity. The angle made by the stream with the line of sight is unknown. The SO_2 channel maps show that the stream seems to maintain its identity down to Doppler velocities of $\sim -3 \text{ km s}^{-1}$, at which point $R \sim 9$ au, but the constant acceleration law seems to be no longer obeyed. A natural explanation is that the stream is born within the slow wind at a space distance from the star of some 12 au, in a region where rotation has essentially faded away. A mechanism such as what Takigawa et al. (2017) call “local acceleration”, caused by locally enhanced density of aluminium-rich dust, would then be at stake. In such a picture, the stream would make a significant but not too large angle with the line of sight, say between 30° and 45° . Qualitatively, this is the most natural and simple interpretation that comes to mind; however, we cannot exclude a configuration where the stream would fly at high velocity near the plane of the sky, not to mention configurations for which the linearity observed in projection is no longer obeyed once de-projected in space.

Figures 12 and 13 show that the stream nearly points to the star; more precisely it points 1.5 ± 1.5 au south-west of the star. Panel c of Figure 13 displays a Position-Velocity (PV) diagram along a ± 3 au wide slit at position angle 140° . An enhancement of intensity is seen back to back to the stream, but at much smaller Doppler velocities. It is shown by a green arrow at position angle 320° in the panels of Figure 10 covering values of R between 0.1 and 0.2 arcsec.

Evidence for important high V_z components in the vicinity of the line of sight crossing the centre of the stellar disc is shown in Figure 14. It displays, for both ^{29}SiO and SO_2 emissions, the high velocity wings of the Doppler velocity spectrum integrated over small circles around the centre of the star ($R < 0.1$ and < 0.2 arcsec), small enough to receive only a small contribution from the blue stream. A Gaussian line centred at the origin and having $\sigma \sim 5.5 \text{ km s}^{-1}$ is shown as reference in the figure. The SO_2 line width is $\sim 15\%$ smaller than the ^{29}SiO line width, probably the result of the steeper r dependence of the flux density. The clear separation observed here between the blue

stream and the high Doppler velocity wings underlines their different nature, the latter being the simple result of line broadening in the inner layer.

4 THE INNER LAYER, ROTATION AND LINE WIDTH

As discussed in Section 3.2, the ^{29}SiO emission of the star and of the inner CSE layer, $R < \sim 12$ au, seems to be seen across a self-absorbing layer moving toward us with a velocity of $\sim 4 \text{ km s}^{-1}$, causing nearly total absorption over its range of Doppler velocities. In order to study the emission of the inner layer, we simply ignore this Doppler velocity interval. Figure 15 shows a PV map, V_z vs ω , in the ring $0.075 < R < 0.175$ arcsec. In each ω bin, the brightness in the V_z absorption interval has been interpolated linearly between its values taken just above and just below. The result is essentially the same as if one keeps the absorbed interval untouched: a fit of the form $A + B \sin(\omega - \omega_0)$ gives $B = 3.6 \text{ km s}^{-1}$ and $\omega_0 = 191^\circ$ instead of 3.6 km s^{-1} and 190° . However, the constant term is now smaller, 0.5 instead of 0.9 km s^{-1} . This shows the robustness of the result in spite of the very strong absorption. We retain a value of $10 \pm 5^\circ$ for the projection angle of the rotation axis, in agreement with the value of $7 \pm 6^\circ$ obtained by Vlemmings et al. (2018).

When averaged over a ring, rotation contributes to broadening the absorption line but does not cause any shift of its mean value. The observed profile should therefore reveal by how much the wind is accelerated, if at all, in the inner layer. We study this with the help of a crude model of the morpho-kinematics of the ^{29}SiO emission of the inner layer. Rotation is assumed to proceed about an axis projecting 10° east of north with a velocity depending on r [arcsec] as $V_{\text{rot}} [\text{km s}^{-1}] = 64r(1 - 4r)$ and $V_{\text{rot}} = 0$ beyond $r = 0.25$ arcsec. The inclination of the rotation axis with respect to the plane of the sky is taken to be 20° . Temperature and density are assumed to depend on distance as $r^{-0.65}$ and r^{-2} respectively, their values at $r = 0.1$ arcsec (6 au), T_0 and n_0 respectively, being varied to optimize the fit. Line broadening is described as a Gaussian of dispersion $\sigma_{\text{turb}} = V_{\text{turb}} \exp[-1/2(r - r_{\text{turb}})^2 / \Delta r_{\text{turb}}^2]$ having itself a Gaussian radial dependence. This line broadening is probably of a complex nature, including shocks from pulsations and convective cell ejections. Its modelling as Gaussian fluctuations is a grossly oversimplified approximation. The best fit, illustrated in Figure 16, gives $n_0 = 130_{-40}^{+90} \text{ molecules cm}^{-3}$ and $T_0 = 450_{-90}^{+130} \text{ K}$: the density is $(40_{-10}^{+30})\%$ and the temperature $(40_{-8}^{+12})\%$ of the values quoted by Van de Sande et al. (2018). The best fit does not allow for significant expansion below

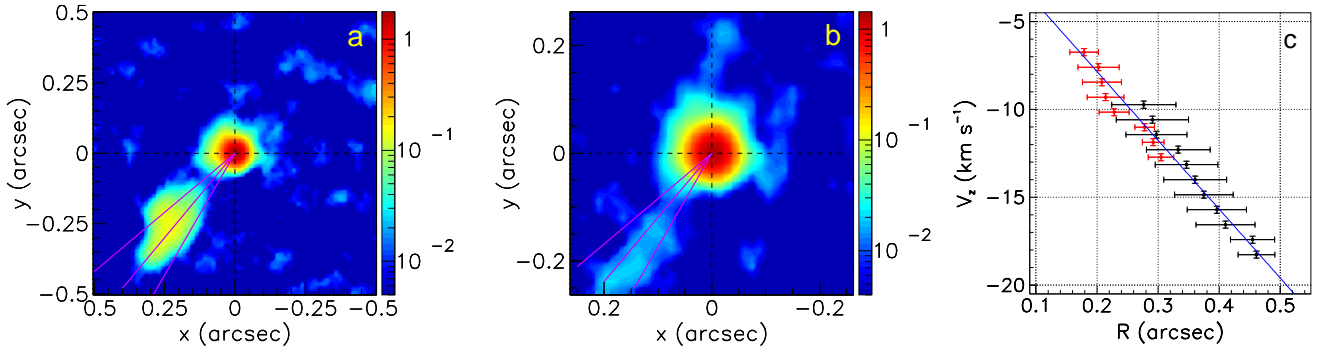


Figure 12. Blue stream. (a): ^{29}SiO intensity map integrated over $-18.7 < V_z < -9.3 \text{ km s}^{-1}$. (b): SO_2 intensity map integrated over $-13.1 < V_z < -6.3 \text{ km s}^{-1}$. On both panels lines mark position angles of 130° , 140° and 150° . The colour scales are in units of $\text{Jy beam}^{-1} \text{ km s}^{-1}$. Note the different spatial scales. (c): Dependence of V_z on R for ^{29}SiO (black) and SO_2 (red) emissions. The line shows the best fit to a form $V_z = kR$ with $k = -39.2 \text{ km s}^{-1} \text{ arcsec}^{-1}$. The dots and error bars show the mean and rms values of R calculated over the blobs seen in the channel maps (Figures A1 and A2).

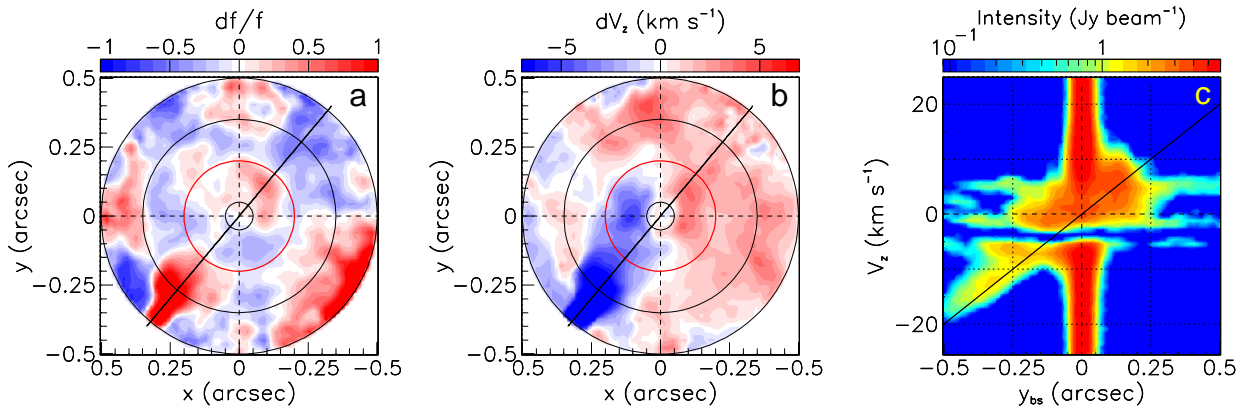


Figure 13. Blue stream in ^{29}SiO emission. (a) relative difference df/f between the ^{29}SiO intensity map and its average over position angle; intensity is integrated over $|V_z| < 20 \text{ km s}^{-1}$. (b) difference dV_z between the ^{29}SiO mean velocity $\langle V_z \rangle$ and its average over position angle; the mean velocity is evaluated over $|V_z| < 20 \text{ km s}^{-1}$. In panels a and b the red circle has a radius of 12 au (0.2 arcsec). (c) PV diagram along the blue stream (position angle of 140° , slit width of $\pm 3 \text{ au}$).

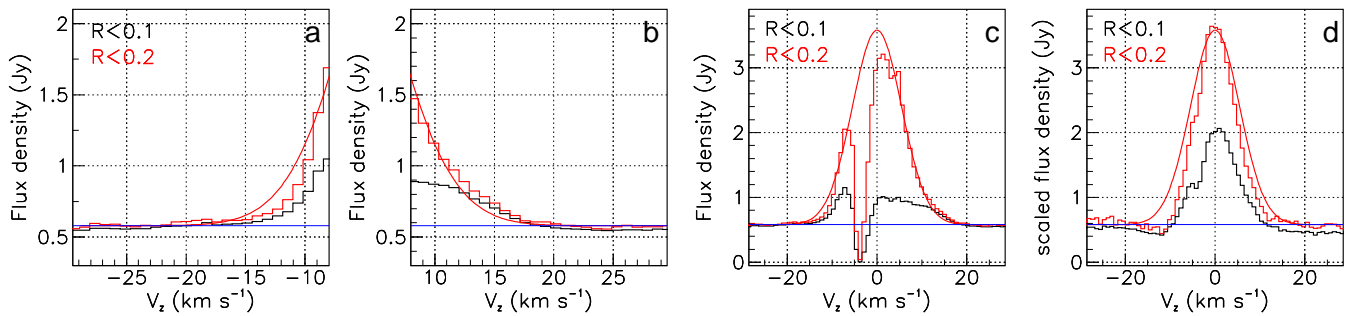


Figure 14. (a) and (b): high velocity wings of the ^{29}SiO Doppler velocity spectrum integrated over small circles around the centre of the star ($R < 0.1$ and < 0.2 arcsec). (c) and (d): total Doppler velocity spectra in the same intervals of R for ^{29}SiO (c) and SO_2 (d). The SO_2 data have been scaled up by a factor 6 and shifted down by 3 Jy for convenience. The Gaussian has an amplitude of 3 Jy above continuum at zero Doppler velocity and a σ of 5.5 km s^{-1} .

$r \sim 10 \text{ au}$ and requires a turbulence confined to the $r < 12 \text{ au}$ region with $V_{\text{turb}} = 4.3 \pm 1.1 \text{ km s}^{-1}$. The assumptions made in the model are qualitatively reasonable but quantitatively somewhat arbitrary and we cannot expect the result to give more than a reference with which to compare the observations. Yet, we can reliably retain that most of the line broadening occurs in the inner layer while most of the radial expansion occurs beyond it. The value obtained for T_0 , about half

the expected value, is probably too low to be blamed uniquely on the crudeness of the model and is likely to have some reality, suggesting a steeper radial dependence than assumed in the model.

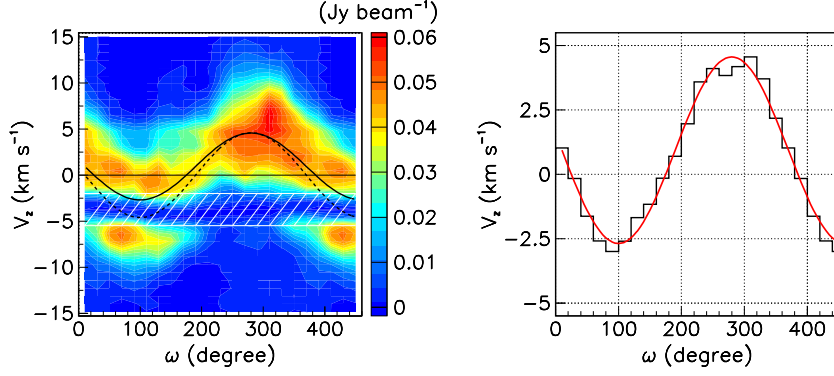


Figure 15. Left: PV map (V_z vs ω) of ^{29}SiO emission in the ring $0.075 < R < 0.175$ arcsec. Right: Dependence on position angle of the mean Doppler velocity averaged over $|V_z| < 12 \text{ km s}^{-1}$. Sine wave fits of $\langle V_z \rangle$ are shown in both panels (full lines). The brightness has been linearly interpolated between $V_z = -5.5$ and $V_z = -2 \text{ km s}^{-1}$ (white striped region in the left panel). Sine wave fit of $\langle V_z \rangle$ with interpolation in the absorption interval is shown in the left panel (dashed line).

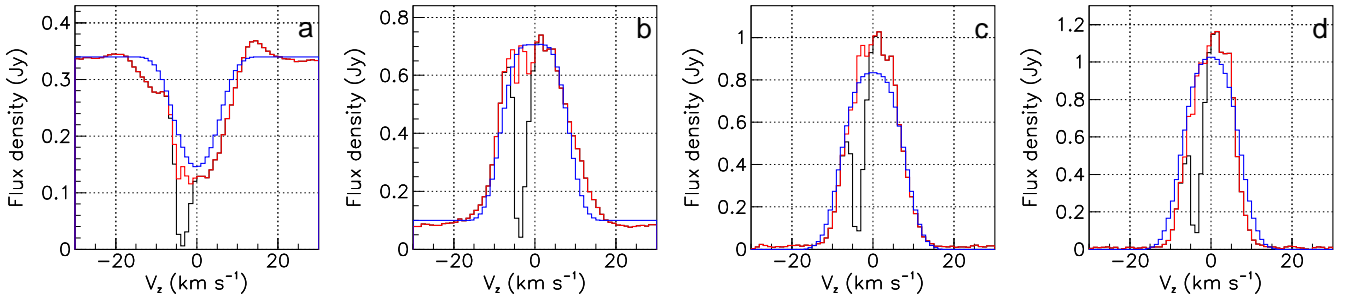


Figure 16. Doppler velocity spectra of $^{29}\text{SiO}(8-7)$ emission: broad components (red) and narrow components (black) of the integrated spectra in the regions $R < 0.035$ (a), $0.05 < R < 0.1$ (b), $0.1 < R < 0.15$ (c), $0.15 < R < 0.2$ (d) arcsec. The blue histograms show the results of the best fit to the broad component.

5 THE BLUE STREAM: A POSSIBLE COMPANION?

Several authors (Homan et al. 2018; Decin et al. 2018; Vlemmings et al. 2018) have entertained the idea that the blue stream might be associated with a low mass companion, probably an evaporating planet. An argument is that the observed star rotation is much too rapid to be a remnant of the rotation of the Main Sequence star and is likely to have received its angular momentum from interaction with a companion. However, such a companion may very well have already been engulfed by the expanding star and have no relation with the observed blue stream, significantly weakening the argument. Vlemmings et al. (2018) locate the companion within 8 au and Homan et al. (2018) at ~ 12 au from the star. The present data show that, in projection on the plane of the sky, gas flows radially from $R_1 \sim 10$ au to $R_2 \sim 30$ au with mean Doppler velocity increasing from $|V_{z1}| \sim 7 \text{ km s}^{-1}$ to $|V_{z2}| \sim 18 \text{ km s}^{-1}$. Calling θ_{bs} the angle between the stream axis and the line of sight, this corresponds in space to a distance $(R_2 - R_1)/\sin \theta_{bs}$ covered at mean velocity $1/2(|V_{z1}| + |V_{z2}|)/\cos \theta_{bs}$ in a time $t = 2(R_2 - R_1)/[(|V_{z1}| + |V_{z2}|)\tan \theta_{bs}] \sim 6.8/\tan \theta_{bs}$ yr. During this time, the companion, assumed to be on a circular orbit of radius $R_1/\sin \theta_{bs}$, covers a distance $d = tV_{orb}$ where $V_{orb}[\text{au yr}^{-1}] = 2\pi\sqrt{(M/M_\odot)\sin \theta_{bs}/R_1[\text{au}]}$ is the orbital velocity; for a star mass $M = 1.4 M_\odot$ (Danilovich et al. 2017; De Beck & Olofsson 2018), $d = 14.6 \cos \theta_{bs}/\sqrt{\sin \theta_{bs}}$ au. As the stream points to the star within ~ 1.5 au, this implies that $\cos \theta_{bs}/\sqrt{\sin \theta_{bs}}$ must not exceed ~ 0.1 or $\theta_{bs} > 84^\circ$. If it were to exceed it the space velocity would exceed 100 km s^{-1} at R_2 .

These simple considerations illustrate the difficulty to describe

the blue stream as gas trailing behind a planetary companion: if the stream flows close to the plane of the sky, one needs a mechanism that boosts the gas velocity radially at a level well above what can be expected from standard acceleration processes; if the stream flows close to the line of sight, the time it takes to cover the distance over which it is detected allows for the companion to cover a distance much larger than acceptable from the good pointing of the stream to the star. This conclusion rests on making a large number of simplifying assumptions. As underlined by Homan et al. (2018), such assumptions may not be obeyed in reality. However, to invalidate the conclusion requires major changes to the picture, not simple numerical adjustments within reasonable limits.

Figure 17 illustrates the geometry. The left panel is drawn in the plane of position angle $\omega_{bs} = 140^\circ$ containing the line of sight and the axis of the blue stream. It is meant to illustrate the dependence of the geometry on the unknown value of θ_{bs} . It is drawn in a configuration where θ_{bs} is small and the blue stream flies close to the line of sight, implying that it starts beyond the inner layer. If instead θ_{bs} were large, the blue stream would fly close to the plane of the sky and would start at the outer edge of the inner layer. As the companion projects at a position angle $\omega_{bs} = 140^\circ$, the inclination θ_R of the orbital axis with respect to the plane of the sky is related to θ_{bs} by the relation $\sin \theta_R = \cos(\omega_{bs} - \omega_R)\sin \theta_{bs}/\sqrt{1 - \sin^2 \theta_{bs} \sin^2(\omega_{bs} - \omega_R)}$, where ω_R is the position angle of the projection of the orbital axis on the plane of the sky. Assuming that the orbital axis is at the same time the rotation axis of the volume of gas we retain a value $\omega_R = 10^\circ \pm 5^\circ$ east of north, from the results listed in Table 3 and those obtained by Vlemmings et al. (2018). To a good approxima-

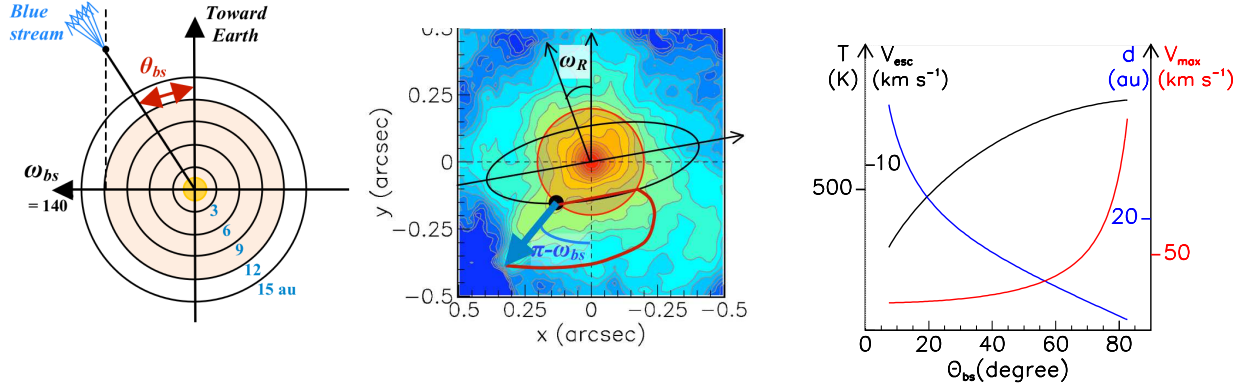


Figure 17. Schematic example of a geometry of the blue stream interpreted as gas trailing beyond an orbiting planet. Left: configuration in a plane containing the line of sight and the companion at the start of the blue stream ($\theta_{bs}=30^\circ$, $\omega_{bs}=140^\circ$, $R=12$ au, $r=24$ au). The rotation area, contained within 12 au from the star, is coloured in orange. Rings of R multiples of 3 au are shown. Centre: sky map showing the companion orbit (black, $\omega_R=10^\circ$, $\theta_R=20^\circ$) and in red the distance covered by the companion in 12 years. The distance covered by the blue stream during the same period is shown as a blue arrow. The red spiral shows the expected density enhancement produced by the gas trailing behind the companion. Right: dependence on θ_{bs} of the temperature (black), the escape velocity (black), the distance d covered by the companion during the time where the blue stream is detected (blue) and the space velocity V_{max} reached by the blue stream gas at $R_2=30$ au (red). Note that escape velocity and temperature have both a $\sqrt{\sin \theta_{bs}}$ dependence and the scales have been chosen for their values to overlap.

tion, the relation reduces to $\theta_{bs}=1.5\theta_R$ implying $\theta_R\sim 20^\circ$ for $\theta_{bs}=30^\circ$, the same value as inferred by Homan et al. (2018) for the rotation axis of the gas volume. Figure 17 (right) shows the dependence on θ_{bs} , at the assumed location of the companion, of the temperature $T[\text{K}]\sim 820\sqrt{\sin \theta_{bs}}$, the escape velocity $V_{esc}[\text{km s}^{-1}]=14\sqrt{\sin \theta_{bs}}$, the distance $d[\text{au}]=14.6\cos \theta_{bs}/\sqrt{\sin \theta_{bs}}$ and the maximal gas velocity (at $R_2=30$ au), $V_{max}[\text{km s}^{-1}]=18/\cos \theta_{bs}$.

Figure 17 invites another comment concerning the radial evolution of the Doppler velocity along the blue stream. When looking only at the projection on the sky plane apparent continuity is observed (Figure 13b) between the central rotation and the stream, suggesting that the acceleration of the stream might be somewhat boosted by the rotation. However, the channel maps do not display such apparent continuity. Indeed, when looking in space, one cannot make sense of such a statement: if the stream flows close to the line of sight, it is born well above the plane of the sky: the rotation velocity is parallel to the line of sight in the plane of the sky but is negligibly small where the stream is born; if it flows close to the plane of the sky, it needs a boost perpendicular to the line of sight and not along it as rotation provides.

6 THE CSE AS PROBED AT LARGER DISTANCES FROM THE STAR

The study of the absorption of ^{29}SiO emission over the stellar disc presented in Section 3.2 has suggested that R Dor is seen across a self-absorbing optically thick layer moving away from the star toward us with a velocity of some 4 km s^{-1} and covering a region of the plane of the sky much larger than the stellar disc. While a similar effect seems to be present in the CSE of W Hya (Takigawa et al. 2017), it has not been explicitly discussed in the literature. The present section addresses this issue in the broader context of a description of the morpho-kinematics of the CSE at distances from the star covering up to some 100 au, where such absorption is expected to take place. Section 6.1 presents a critical discussion of possible instrumental effects, in particular related to the short spacing problem (Gueth et al. 1997), which might mimic the extension beyond the stellar disc of the absorption of the ^{29}SiO emission. The following sections probe the

CSE using emissions of the $\text{SO}(J_K=6_5-5_4)$ line, together with three other molecular lines: ^{28}SiO , CO and HCN. The emission of the SO line was studied in Paper I; Section 6.2 recalls the main results and presents a new and detailed description of the space morphology. The emission of the other lines was studied in much less detail in Paper I and Section 6.3 presents a qualitative picture of the morpho-kinematics as obtained from these multiline observations; Section 6.4 addresses the specific issue of absorption.

6.1 Absorption of the ^{29}SiO line emission beyond the stellar disc

Figure 11 has given evidence for strong absorption of the ^{29}SiO line emission to persist well beyond the stellar disc. In order to get an idea of which absorption to expect from the antenna configuration used for the observations, we construct a very crude model that reproduces qualitatively the main characteristics of the ^{29}SiO morpho-kinematics. It assumes the isotropy of the brightness in the plane of the sky and considers three different models, each defined by a simple radial dependence of the brightness as illustrated in Figure 18a. It considers three different brightness distributions on the plane of the sky. The first model, case 1, shown in blue, represents continuum emission and is described as a uniform brightness of 1 Jy/pixel over the stellar disc ($R<0.04$ arcsec). The second model, case 2, in red, shows a disc of uniform brightness, arbitrarily set to 0.1 Jy/pixel, and having a radius of 0.3 arcsec, meant to represent the emission of the CSE. Emission is completely absorbed over the stellar disc; this case is meant to mimic the real situation in the frequency channel corresponding to a Doppler velocity of -4 km s^{-1} . The third model, case 3, shown as a thick black line, represents instead the situation in the frequency channel corresponding to $V_z=+4\text{ km s}^{-1}$, expected to detect the same emission as the -4 km s^{-1} channel but without absorption over the stellar disc: emission is not absorbed and is described by a uniform brightness of 1 Jy/pixel over the stellar disc. The emission in case 3 is the sum of that in cases 1 and 2. For each of the three cases, we produce³ visibilities U corresponding to the actual antenna configuration illustrated in Figure 2. Figure 18b displays the

³ Using SIMOBSERVE in CASA, <http://casa.nrao.edu>

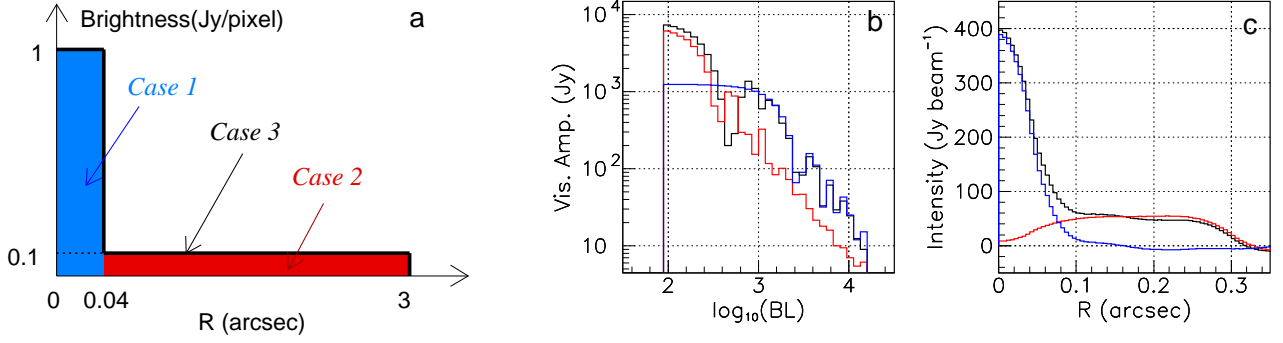


Figure 18. (a) Radial dependence of each of the three model brightness used in the evaluation of the corresponding visibilities (see text). (b) Dependence of the amplitude of the visibility on the decimal logarithm of the baseline lengths (meters) for each of the three cases 1 (blue), 2 (red) and 3 (black). (c) R distributions of the flux density as evaluated from the dirty maps obtained from the model visibilities.

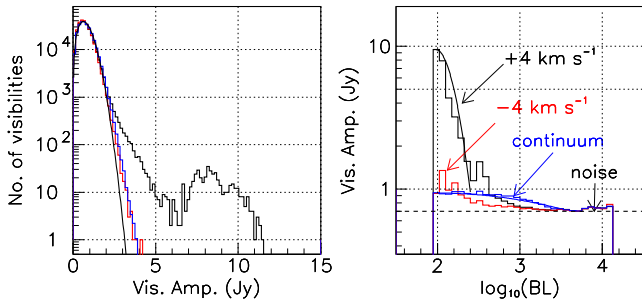


Figure 19. Visibilities measured from the ²⁹SiO observations. In both panels colours identify the velocity intervals defined in the text: blue for continuum (normalized to a single frequency channel), red for -4 km s^{-1} and black for $+4 \text{ km s}^{-1}$. Left: distribution of the amplitude of the observed visibility U averaged over each of the frequency intervals described in the text; the fits correspond to Gaussian distributions for each of the real and imaginary parts of U . Right: normalised visibility distributions for each of the three frequency intervals as a function of the decimal logarithm of the baseline length (m).

baseline dependence of the visibility amplitude for each of the three cases. Case 1, meant to represent continuum, covers long baselines, up to $\sim 1000 \text{ m}$, with small visibilities (in spite of its larger brightness than the gas, by a factor 10, it covers a much smaller area, by a factor 130). Case 2, meant to represent $V_z = -4 \text{ km s}^{-1}$, shows that the gas emission is indeed absorbed, but only over a small distance from the star, not exceeding $\sim 0.1 \text{ arcsec}$, in strong contrast with what we observe in the real case (Figure 19). Case 3, meant to represent $V_z = +4 \text{ km s}^{-1}$, shows the gas emission that covers short baselines, up to $\sim 500 \text{ m}$, but with large visibilities. In summary, in spite of the poor uv coverage at short baselines, we expect absorption to extend only slightly beyond the stellar disc, well below the maximal recoverable scale, in sharp contrast with observation.

Turning now to the actual ²⁹SiO observations, we select the two frequency intervals covering $V_z = \pm 4 \text{ km s}^{-1}$ and define a third interval, meant to measure continuum emission, made of two sets of 9 frequency channels each (7.7 km s^{-1}) at the beginning and end of the frequency band. The left panel of Figure 19 displays the distributions of the measured visibility amplitude, $|U|$, averaged over these intervals. The noise is well described by a form $|U| \exp(-1/2 |U|^2 / \sigma^2)$, meaning a Gaussian distribution in each of $\text{Re}(U)$ and $\text{Im}(U)$ with a common rms value, σ , measured to be 0.62 Jy . While the measured visibilities are large in the gas layer surrounding the star (black), they are much smaller and closer to the noise for the continuum (blue) and

the maximal absorption channel (red). The right panel of Figure 19 shows the dependence on baseline of the visibility for each frequency interval separately, again normalised to the baseline distribution of Figure 2c. Continuum emission (blue), corresponding to the stellar disc, covers the broader range of baselines, extending up to $\sim 2.3 \text{ km}$; gas emission (black), corresponding to the gas envelope around the star, covers up to baselines of $\sim 500 \text{ m}$. Finally, the red histogram is expected to stay at noise level down to baselines of $\sim 500 \text{ m}$, the disc region being nearly completely absorbed, and it does so. However, toward lower baselines, it is expected to rise near the level of the black histogram, as happens for case 2 in Figure 18b, but in fact it reaches much lower a level: this shows that the effect is already present at the level of the measured visibilities.

The short spacing problem is precisely the same for the $V_z = +4 \text{ km s}^{-1}$ and $V_z = -4 \text{ km s}^{-1}$ cases; the noise is the same; the calibration uses only observations made for this purpose and is also the same for the two channels. The global blank out of the $V_z = -4 \text{ km s}^{-1}$ observations is therefore shown to be present at raw data level already and we must conclude that it is real and not the result of some instrumental artefact.

6.2 Overall picture of the morpho-kinematics as seen from SO emission

Paper I has presented a detailed study of the morpho-kinematics of the CSE using ALMA observations of the emission of the SO($J_K = 6_5 - 5_4$) line of which channel maps were displayed in the supplementary material. These are from project 2017.1.00824.S observed in December 2017 in band 6 with an average of 45 antennas. Distances from the star reaching up to some $\sim 120 \text{ au}$ are probed with a circular beam of 9 au FWHM . Evidence is obtained for a slow radial wind with Doppler velocities reaching up to $\sim 6 \text{ km s}^{-1}$, displaying significant anisotropy and inhomogeneity.

The complexity of the morphology of the CSE makes it difficult to draw simple 2-D representations of the data cube. We find that PV maps displaying the brightness in the Doppler velocity (V_z) vs position angle (ω) or vs projected distance (R) planes, are particularly convenient for this purpose. They have the advantage that a wind blowing at constant velocity V in a small solid angle appears as a small clump in the former and as a stretch of uniform density in the latter. Moreover, for an isotropic wind of constant and uniform radial velocity V , the angle φ of the flow with the line of sight is simply obtained from the relation $V_z = V \cos \varphi$, providing an evaluation of $z = R / \tan \varphi$ and therefore of the morpho-kinematics in space. More

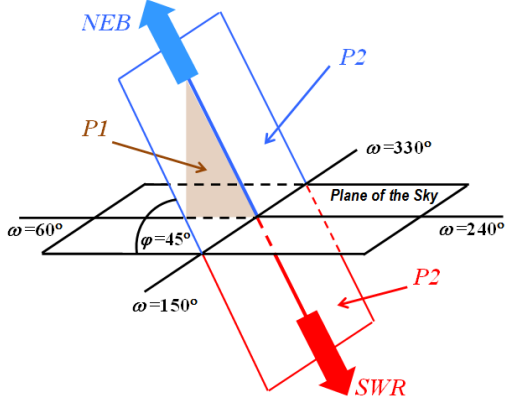


Figure 20. Outflow geometry (see text).

generally, space reconstruction can be done as long as the dependence of V on r is known; in particular for an acceleration law of the form $V=V_{\text{term}}r/(r+r_{1/2})$, tending asymptotically to the terminal velocity V_{term} when r tends to infinity and reaching the value $1/2V_{\text{term}}$ for $r=r_{1/2}$, one has $r=[\alpha^2r_{1/2}+\sqrt{\alpha^4r_{1/2}^2+(1-\alpha^2)(R^2+\alpha^2r_{1/2}^2)}]/(1-\alpha^2)$ with $\alpha=V_z/V$.

The quality of the SO observations is excellent and the CSE is optically thin enough to suffer no significant absorption. They show two nearly back-to-back outflows, one (NEB) covering the north-eastern blue-shifted octant of the data cube and the other (SWR) the south-western red-shifted octant. Figure 20 shows the geometry. Figure 21a displays the intensity in the V_z vs ω plane for $12 \text{ au} < R < 60 \text{ au}$. A very crude model of two back-to-back outflows is used to evaluate the orientation of the common outflow axis: it projects on the plane of the sky $60^\circ \pm 5^\circ$ east of north. Both SWR and NEB have a multicore structure. We use two planes on which to project the emission of the outflows. They are perpendicular to each other and cross on the outflow axis (Figure 20). Plane P1 is perpendicular to the plane of the sky and projects on it at 60° position angle. Plane P2 crosses the plane of the sky at $60^\circ + 90^\circ = 150^\circ$ position angle. The angle φ of the outflow axis with the plane of the sky depends on the acceleration of the flow. Using the law introduced in the preceding paragraph with $V_{\text{term}}=7 \text{ km s}^{-1}$ and $r_{1/2}=30 \text{ au}$ (0.5 arcsec) the map of the intensity projected on P1, displayed in panel b of Figure 21, gives $\varphi \sim 45^\circ$. The value of $r_{1/2}$ can be chosen anywhere between 0.25 and 0.75 arcsec (15 and 45 au) without φ changing by more than $\pm 5^\circ$. Panel c of the figure shows the map of the intensity projected on P2.

When looking at the radial distribution of the intensity, significant inhomogeneity is observed. Figure 21d displays the distribution of the intensity in the V_z vs R plane, integrated over all position angles. It was shown in Paper I to reveal the presence of a ring cavity surrounding the star, approximately perpendicular to the outflow axis, seen as a hole of emission at $R \sim 0.5$ arcsec. A second hole at $R \sim 1.1$ arcsec is also visible. This was interpreted in Paper I as evidence for episodes of enhanced mass loss. However, the ring cavity receives important contribution from the waist separating the outflows: understanding its precise nature requires additional observations.

Table 4. Parameters of line emission per arcsec. A is the Einstein coefficient, J is the spin of the upper level, f is the frequency, λ is the wavelength, ΔE is the transition energy, E_u is the energy of the upper level, n is the number density, r_0 is the radius up to which the relative abundance is constant, σ_0 describes its radial decline as a Gaussian centred at r_0 and having a σ equal to σ_0 . T is the temperature, $F_r=4\pi kAn(2J+1)e^{-E_u/T}/T$ is the emission in a shell of 1 arcsec radius with k accounting for the different partition functions.

Molecule	^{28}SiO	CO	HCN	SO
A [10^{-4}]	22.0	0.025	20.5	1.93
$2J+1$	17	7	9	13
k [10^5]	3.3	9.2	6.9	0.97
f [GHz]	347.3	345.8	354.5	251.8
λ [mm]	0.864	0.867	0.846	1.191
ΔE [K]	16.7	16.7	17.1	12.1
E_u [K]	75	33	43	51
$n/n(\text{H}_2)$ [10^{-4}]	0.6	2	0.005	0.07
r_0 [arcsec]	1.5	10	0	0
σ_0 [arcsec]	1.1	5	1.6	1.1
F_r [$\text{Jy km s}^{-1} \text{ arcsec}^{-1}$] @ $T=150 \text{ K}$, $r=1 \text{ arcsec}$	24080	138	210	44

6.3 Overall picture of the morpho-kinematics from a comparison between SO, ^{28}SiO , CO and HCN line emissions

In the present section we use the emission of lines $^{28}\text{SiO}(8-7)$, $\text{CO}(3-2)$ and $\text{HCN}(4-3)$ to probe the CSE. They were previously considered in Paper I and have been briefly introduced in Section 2. Figures 22 and 23 describe the main results. Doppler velocity spectra measured over the stellar disc (Figure 22a) show nearly total absorption of the ^{28}SiO line at $V_z \sim -4 \text{ km s}^{-1}$, confirming the results obtained for the ^{29}SiO isotologue when accounting for the much broader beam (FWHM ~ 7 stellar radii). They also show significant but much smaller absorption of the HCN and CO lines. The CO line emission is absorbed at lower Doppler velocity than the SiO line, nearly -6 km s^{-1} instead of -4 km s^{-1} : this is probably the result of its much larger radial extension; it suggests that the wind acceleration from 4 km s^{-1} to the terminal velocity of $\sim 6 \text{ km s}^{-1}$ is significant in a region where the density ratio between SiO and CO molecules is declining, namely beyond $r \sim 1$ arcsec but the quality of the data does not allow for a more quantitative statement. Figure 22b displays Doppler velocity spectra outside the stellar disc where some absorption of the ^{28}SiO line emission is seen to persist. Figure 22c,d displays, for the blue and red hemispheres separately, the radial distributions of the flux density integrated over Doppler velocity using the radial dependence of the velocity introduced in Section 6.2 for SO emission ($r_{1/2}=0.5$ arcsec). If the CSE were optically thin, its emission would be simply described by the ε parameter. Using abundances relative to H_2 given by Van de Sande et al. (2018) and Danilovich et al. (2016) and an H_2 density corresponding to a mass-loss rate of $\sim 1.6 \cdot 10^{-7} M_\odot \text{ year}^{-1}$ as was done in Section 3.2, we calculate its value (Table 4) for a temperature of 150 K and a distance of 1 arcsec from the star and obtain the emission F_r of a shell of 1 arcsec radius with which to compare the observations displayed in Figure 22c,d. We find that the SO and HCN observed emissions are well predicted and the CO emission some 30% below prediction, which suggests that absorption is small for these lines (but in the blue hemisphere, HCN seems to suffer significant absorption). However, the observed ^{28}SiO emission is considerably smaller, suggesting very strong self-absorption.

Figure 23 compares the ^{28}SiO , CO and HCN emissions to SO emission by displaying the same distributions as displayed in Figure

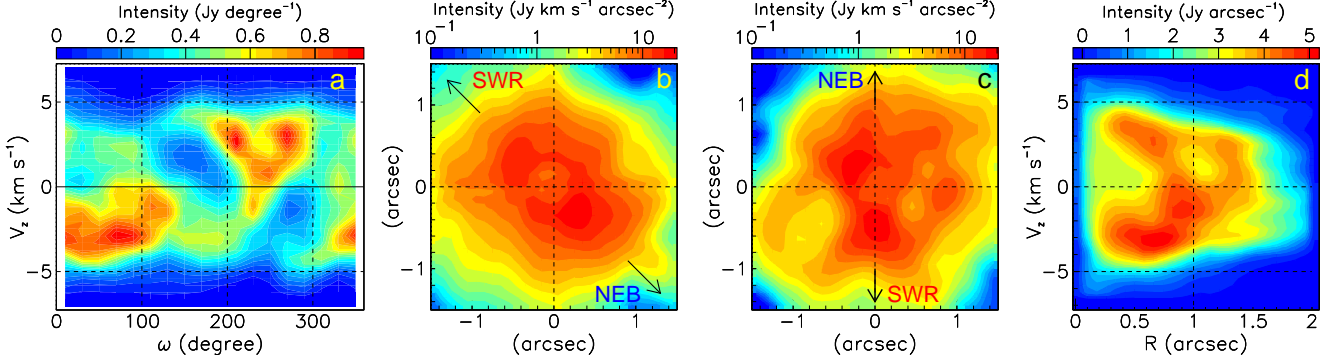


Figure 21. SO($J_K=6_5-5_4$) line emission. (a): intensity in the V_z vs ω plane integrated over $12 \text{ au} < R < 60 \text{ au}$. (b): intensity projected on P1; up-left (down-right) points to SWR (NEB). (c): intensity projected on P2; up (down) points to NEB (SWR). In both panels (b) and (c) a cut $r > 0.3 \text{ arcsec}$ (18 au) has been applied. (d): intensity projected on the V_z vs R plane, integrated over position angles.

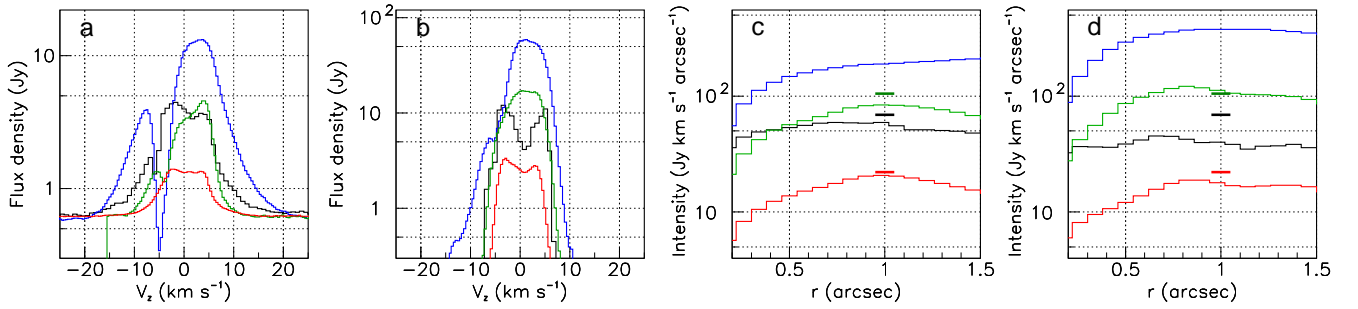


Figure 22. Doppler velocity spectra (Jy) integrated over ω and $R < 0.3 \text{ arcsec}$ (a) or $0.3 < R < 1.0 \text{ arcsec}$ (b). (c) and (d): r distributions evaluated using the velocity law described in Section 6.2 for $V_z < 0$ (c) and $V_z > 0$ (d). The coloured horizontal lines show the values of $1/2 F_r$ (accounting for the split in two hemispheres) calculated for a temperature of 150 K in the optically thin approximation. The values predicted for ^{28}SiO in this approximation are considerably larger than observed and off-scale in the figure. In all panels SO is red, ^{28}SiO blue, CO black and HCN green.

21 for the latter. While CO and HCN emissions show qualitatively similar distributions as SO, ^{28}SiO seems to display a significantly different morphology. This had been noted in Paper I but the information contained in Figure 23 offers a more detailed description of the differences at stake. The V_z vs ω map (panel a) shows a slight depression rather than enhancement of emission at the position angle of the south-western outflow, $\omega \sim 240^\circ$. When seen in the outflow planes (panels b and c) the emission shows no sign of an outflow but looks instead as isotropic, simply absorbed in the blue hemisphere. The same picture is suggested by the V_z vs R maps displayed in the right panels where the larger radial extension of the CO emission plays an important role. In order to explain such significant differences between the ^{28}SiO emission and that of the other lines, we need to understand the impact of the strong self-absorption.

6.4 Absorption of SiO emission

The comparison of the observed ^{28}SiO emission with the calculated value of the unabsorbed emission parameter ε performed in the preceding section suggests a strong self-absorption in both the red and blue hemispheres. In an idealised LTE picture, the emission reads $I = \varepsilon(1 - e^{-\tau})/\tau$ and the optical thickness is $\tau = 2.9 \cdot 10^7 \varepsilon (e^{\Delta E/T} - 1)/f^3$. The ratio τ/ε is nearly the same for all lines: at 150 K, it is ~ 0.08 , 0.08 , 0.08 and 0.15 for SiO, CO, HCN and SO respectively. Namely, for a 0.1 arcsec thick layer, $\tau = 15$, 0.09 , 0.13

and 0.05 at 150 K and $r = 1 \text{ arcsec}$, meaning an effective absorption by a factor ~ 15 for SiO.

Another comparison of relevance is between the best fit to the ^{29}SiO emission in a ring $0.15 < R < 0.20 \text{ arcsec}$ obtained in Section 4 and the emission predicted using the same model for a density increased by a factor $1/0.08$. We find that the ratio of absorbed to non-absorbed emissions decreases from 0.48 for the ^{29}SiO density to 0.062 for the increased density, namely an increase of the absorption by a factor ~ 7.7 . Figure 24 compares the R distributions of the emission of both isotopologues, the ^{29}SiO data having been smeared to account for the larger ^{28}SiO beam size and the ^{28}SiO data having been multiplied by 0.08 to account for the isotopic ratio. The observed increase of absorption between ^{29}SiO and ^{28}SiO is ~ 5 in the red hemisphere and ~ 10 in the blue hemisphere, well bracketing the predicted value of 7.7 .

Finally, we model the ^{28}SiO emission over two rings, $0.35 < R < 0.55 \text{ arcsec}$ and $0.65 < R < 0.85 \text{ arcsec}$, far enough from the stellar disc for continuum emission to be negligible. The model includes the same form of Gaussian line broadening as described in Section 4 with the addition of a constant width V_{turb0} . The radial expansion has the form described in Section 6.2. It assumes a r^{-2} radial dependence of the density. The temperature is taken of the form $T = T_{0.5} r^{-p}$. The parameters being adjusted are the expansion parameter $r_{1/2}$, the density $N_{0.5}$ at $r = 0.5 \text{ arcsec}$, the line width parameters and the temperature parameters $T_{0.5}$ and p . The result is shown in panels c and d of Figure 24. The fit requires again a much steeper radial dependence of the

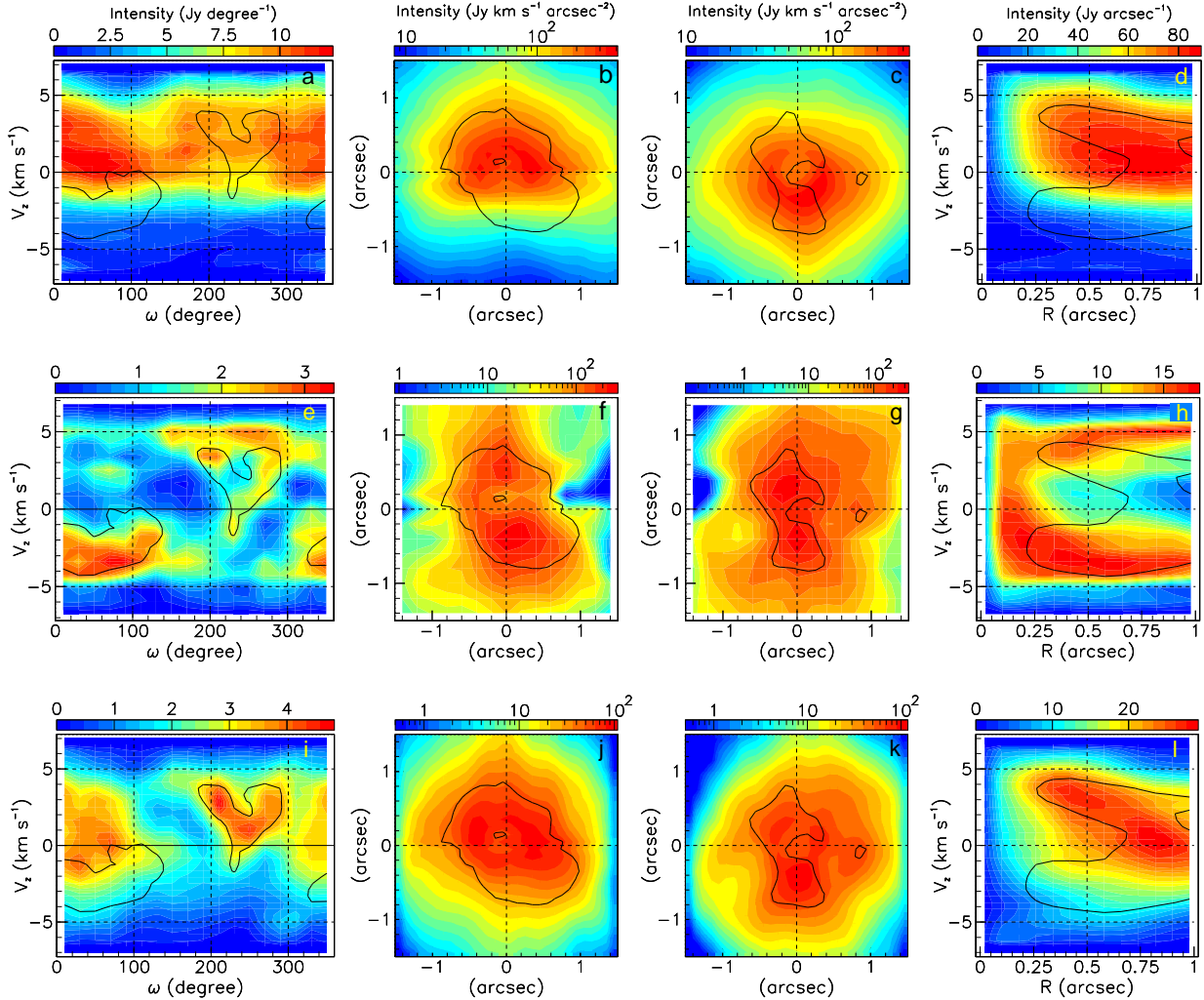


Figure 23. ^{28}SiO (upper row), CO (middle row) and HCN (lower row) line emissions. Left: projection on the V_z vs ω plane integrated over $12 \text{ au} < R < 60 \text{ au}$. Centre-left: projection on P1. Centre-right: projection on P2. Right: projection on the V_z vs R plane, integrated over position angles. Units are as in Figure 21 from which the contour of SO emission at $\sim 60\%$ maximum is shown as reference in each panel.

temperature than used in earlier works: the fits displayed in Figure 24 are for $T_{0.5}=315 \text{ K}$ and a $1/r$ dependence ($p=1$) meaning $T=158 \text{ K}$ at $r=1 \text{ arcsec}$. The model is too simple and makes too many simplifying assumptions for these numbers to be taken at face value. Yet, the trend for a steep radial dependence of the temperature, which was already suggested by the study of the inner layer presented in Section 4, is likely to be qualitatively valid. The best fit value of $r_{1/2}$ is 0.4 arcsec and the fit is not very sensitive to its precise value. The line broadening is the sum of a constant term, $V_{\text{turb}0}=0.7 \text{ km s}^{-1}$, and a Gaussian of amplitude 2 km s^{-1} centred at $r=0.3 \text{ arcsec}$ and having a σ of 0.20 arcsec . The density at $r=0.5 \text{ arcsec}$ is $1625 \text{ molecules per cm}^3$, in agreement with the value found for the ^{29}SiO fit, $\sim 40\%$ of that given by Van de Sande et al. (2018). Better fits than shown in Figure 24 can be obtained by fine-tuning the forms adopted for the radial dependence of the various parameters, but we refrain from showing these because the crudeness of the model makes such an exercise pointless.

Qualitatively, the several arguments developed in the present and preceding sections have all shown that the SiO layer covering from $\sim 0.2 \text{ arcsec}$ to $>1 \text{ arcsec}$ distance from the star is optically thick and absorbs a large fraction of its own emission in both the red and

blue hemispheres. The observed strong absorption is a result of the concurrence of a large Einstein coefficient and a large abundance: it is not expected to be specific to R Dor but should be also present in other oxygen-rich AGB stars. It is indeed the case, at least qualitatively, for Mira Ceti (Wong et al. 2016) and W Hya (Takigawa et al. 2017). A quantitative reliable modelling would require observations of higher sensitivity and better uv coverage than currently available.

7 SUMMARY AND CONCLUSIONS

The observations presented and analysed in the present article contribute important new information on five major features of the morpho-kinematics of the CSE of R Dor: rotation, absorption, presence of a south-eastern blue-shifted stream, large Doppler velocity wings and the detailed structure of the CSE up to $\sim 60 \text{ au}$ distance from the star.

i) Rotation is seen to reach a maximal velocity of ~ 5 to 7 km s^{-1} at some $8 \pm 2 \text{ au}$ from the centre of the star, where the Keplerian orbital velocity around a $1.4 M_{\odot}$ star is $\sim 13 \text{ km s}^{-1}$. Its axis projects on the plane of the sky at a position angle of $10 \pm 5^{\circ}$ and makes an

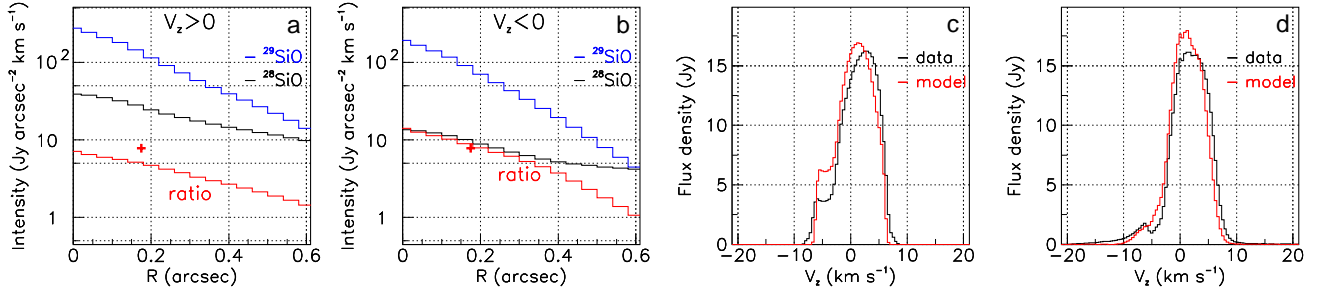


Figure 24. (a) and (b): R distributions in the red (a) and blue (b) hemispheres of the ^{29}SiO emission smeared with the ^{28}SiO beam (blue) and the ^{28}SiO emission multiplied by 0.08 (black); their ratio is shown in red. Continuum is not subtracted and the MRS of ^{29}SiO is only 0.36 arcsec, that of ^{28}SiO is 1.3 arcsec. The cross shows the increase of the absorption predicted by the model in a ring $0.15 < R < 0.20$ arcsec when increasing the ^{29}SiO density by a factor 1/0.08 (see text). (c) and (d): ^{28}SiO Doppler velocity spectra (black) in rings $0.35 < R < 0.55$ arcsec (c) and $0.65 < R < 0.85$ arcsec (d) are compared with the crude model calculation (red) described in the text.

unknown angle with the plane of the sky; yet, qualitative considerations favour a low value, typically $20^\circ \pm 20^\circ$ as suggested by the analysis of Homan et al. (2018). The picture obtained from the analysis of the present observations reconciles those presented earlier by Vlemmings et al. (2018) and Homan et al. (2018), claimed to be in conflict by the former authors. Qualitatively, it confirms an increase of the rotation velocity from $\sim 1 \text{ km s}^{-1}$ at the surface of the star to its maximal value, described by Vlemmings et al. (2018) as “solid body rotation”; and it confirms the decrease of the rotation velocity from its maximal value down to zero around ~ 15 au, described by Homan et al. (2018) as “sub-Keplerian”. Quantitatively, evidence is given for an important contribution of the blue stream to the kinematics for projected distances from the star exceeding ~ 12 au, giving the appearance of a larger rotation velocity. Both ^{29}SiO and SO_2 emission data give very consistent results. An interpretation suggested by Vlemmings et al. (2018) is the presence of a companion at some 6 au from the star, resulting in solid-body rotation of the close-by atmosphere extending up to a very few stellar radii and decreasing beyond. It might equally be that such a companion has already been engulfed in the recent past. The morphology of the rotating volume does not show strong anisotropy and, in particular, fails to provide evidence for a disc-like flattening about the equator as suggested by Homan et al. (2018). It shows instead a broad enhancement covering the north-western quadrant, reaching close to 20% for ^{29}SiO and to 30% for SO_2 .

ii) Absorption of the ^{29}SiO emission is nearly total at $V_z \sim -4 \text{ km s}^{-1}$ over the stellar disc and extends beyond it, an observation that had not been explicitly made in earlier studies. Strictly speaking, total absorption is not possible because one cannot prevent the outer part of an optically thick layer from shining. Quantitatively, using as reference the prediction of a simple LTE model, it would require the presence of a low temperature self-absorbing layer, expanding with a velocity of $\sim 4 \text{ km s}^{-1}$ at a distance exceeding some 40 au from the star. A detailed study of the morpho-kinematics of the CSE at distances reaching ~ 100 au, using ALMA observations of SO , ^{28}SiO , CO and HCN suggests that such is indeed the case. New observations of higher sensitivity and better uv coverage are needed to reliably confirm this important result. A qualitatively similar effect is expected to occur in the environment of other oxygen-rich AGB stars, as seems indeed to be the case for Mira Ceti and W Hya.

iii) The blue stream is observed at $\sim 140^\circ$ position angle to extend radially from ~ 10 au to ~ 30 au with a mean projected acceleration of $39.2 \pm 0.9 \text{ km s}^{-1} \text{ arcsec}^{-1}$. Interpreted as a gas stream in rectilinear motion, it points to the star to within some 1.5 au. This makes it

difficult to describe it as gas trailing beyond a possible companion: unless it flows near the plane of the sky, its trajectory covers too long a time during which the companion is expected to travel too long a distance: it should have the shape of a spiral rather than of a straight line and should therefore not be seen to point precisely to the star. If instead it flows close to the plane of the sky, it must reach very large space velocities, up to 100 km s^{-1} or so. It is difficult to conceive a sensible scenario that would simply relate the presence of the blue stream to that of an evaporating planetary companion, as suggested earlier by Decin et al. (2018); Homan et al. (2018) and Vlemmings et al. (2018). Qualitatively, as the blue stream is seen in continuity with the expansion of the slow wind, a more natural interpretation of its dynamics is that it is associated with a local enhancement of aluminium-rich dust density at some 12 au from the star and some 30° to 45° from the line of sight (Takigawa et al. 2017).

The absence of evidence for a planetary companion should not be interpreted as evidence for the absence of such companions. Indeed, it would be unreasonable to ignore that AGB stars are very likely to host many planets in their CSE, as do the parent Main Sequence stars. However, while the engulfment process is expected to be extremely fast (Villaver et al. 2014, and references therein) we must remember that the dust mass around R Dor is two orders of magnitude smaller than the Earth mass (Decin et al. 2018) and many events may happen before and during engulfment that might leave a mark in the CSE.

iv) The high Doppler velocity wings studied earlier have been shown to be well separated from the blue stream and to be caused by a significant line broadening occurring within the inner layer of the CSE, below 12 au from the star. Its precise nature, including turbulence, shocks and even a possible effect of pulsations, remains to be clarified.

v) The presence of two broad outflows covering the south-western red-shifted and north-eastern blue-shifted octants respectively has been confirmed and parameters defining their morpho-kinematics have been estimated. Observation of other lines, from ^{28}SiO , CO and HCN molecules, probing the CSE up to some 60 au from the star, has provided a qualitative confirmation of the SO result. However, the observed morpho-kinematics of ^{28}SiO emission differs significantly from that of the other lines, probably because the very strong self-absorption hides the inner layers from observation. New observations with good uv coverage, resolution and sensitivity, are very much needed in order to refine the general picture obtained from the existing SO observations.

The picture of the R Dor CSE that emerges from the present study

is consistent with an early launch of the wind by aluminium-rich dust, followed by a progressive increase of the contribution of silicon-rich dust, giving support to a three-step picture of the generation and acceleration of the wind: in a first step pulsations and convective cell ejections give a first boost to the gas, with velocities reaching typically some 10 km s^{-1} , sufficient to eject part of it to a few au beyond the photosphere. There, in a second step, large transparent grains start to condense, mostly aluminium-rich, reaching grain sizes of a few tenths of a micron within some 10 au from the star; they are accelerated by photon scattering and transfer part of their momentum to the gas, providing a first pre-acceleration that brings it into a region where silicate grains start to condense. These grains are accelerated by radiation pressure and reach up to several tens au beyond the star surface. There, in a third step, the gas is progressively accelerated by collisions with the dust grains to reach a terminal velocity at the 5 to 10 km s^{-1} scale at some 100 au from the star, where it has finally escaped the star gravity.

Yet, to make sense of what we observe, we need to answer a number of open questions concerning the possible presence of planetary companion(s) and its impact, the mechanism causing the generation of significant rotation, the precise nature of the blue-shifted stream and the mechanism beyond the shaping of the pair of back-to-back outflows. In particular, new observations with good *uv* coverage, resolution and sensitivity, of line emissions probing the CSE up to some 60 au from the star, such as ^{28}SiO , CO and HCN molecules, are very much needed in order to refine the general picture obtained from the existing SO observations.

We are still a long way away from being able to model precisely the physics and chemistry at stake in the CSE of R Dor. Such modelling cannot afford to ignore the complex reality of the observed morphokinematics. While progressing in its description, we still fail to give a coherent interpretation of three apparently unrelated features: star rotation, blue stream and pair of broad back-to-back outflows.

ACKNOWLEDGEMENTS

We express our deep gratitude to the anonymous referee for a very detailed and pertinent review that helped to significantly improve the presentation of the manuscript and we thank Professors Eva Villaver, Leen Decin, Ward Homan, Pierre Lesaffre and Stéphane Guilloteau for useful discussions. This paper makes use of the following ALMA data: ADS/JAO.ALMA#2017.1.00191.S (PI: Theo Khouri), ADS/JAO.ALMA#2017.1.00824.S (PI: Leen Decin) and ADS/JAO.ALMA#2013.1.00166.S (PI: Leen Decin). ALMA is a partnership of ESO (representing its member states), NSF (USA) and NINS (Japan), together with NRC (Canada), MOST and ASIAA (Taiwan), and KASI (Republic of Korea), in cooperation with the Republic of Chile. The Joint ALMA Observatory is operated by ESO, AUI/NRAO and NAOJ. The SO data are retrieved from the JVO/NAOJ portal. We are deeply indebted to the ALMA partnership, whose open access policy means invaluable support and encouragement for Vietnamese astrophysics. In particular, we acknowledge the time and effort dedicated by the PIs of the projects used in this article for producing proposals of observations selected to best serve the AGB community. Financial support from the World Laboratory, the Odon Vallet Foundation and VNSC is gratefully acknowledged. This research is funded by the Vietnam National Foundation for Science and Technology Development (NAFOSTED) under grant number 103.99-2019.368.

DATA AVAILABILITY

The raw data are available on the ALMA archive ADS/JAO.ALMA#2017.1.00191.S, ADS/JAO.ALMA#2017.1.00824.S, ADS/JAO.ALMA#2013.1.00166.S. The calibrated and imaged data underlying this article will be shared on reasonable request to the corresponding author.

REFERENCES

- Bedding T. R., Zijlstra A. A., Jones A., Foster G., 1998, *MNRAS*, **301**, 1073
 Danilovich T., De Beck E., Black J. H., Olofsson H., Justtanont K., 2016, *A&A*, **588**, A119
 Danilovich T., Lombaert R., Decin L., Karakas A., Maercker M., Olofsson H., 2017, *A&A*, **602**, A14
 Danilovich T., Richards A. M. S., Karakas A. I., Van de Sande M., Decin L., De Ceuster F., 2019, *MNRAS*, **484**, 494
 Danilovich T., Richards A. M. S., Decin L., Van de Sande M., Gottlieb C. A., 2020, *MNRAS*, **494**, 1323
 De Beck E., Olofsson H., 2018, *A&A*, **615**, A8
 Decin L., et al., 2017, *A&A*, **608**, A55
 Decin L., Richards A. M. S., Danilovich T., Homan W., Nuth J. A., 2018, *A&A*, **615**, A28
 Dumm T., Schild H., 1998, *New Astron.*, **3**, 137
 Freytag B., Liljegren S., Höfner S., 2017, *A&A*, **600**, A137
 Gueth F., Guilloteau S., Dutrey A., Bachiller R., 1997, *A&A*, **323**, 943
 Heras A. M., Hony S., 2005, *A&A*, **439**, 171
 Hoai D. T., Nhung P. T., Tuan-Anh P., Darriulat P., Diep P. N., Phuong N. T., Thai T. T., 2020, *Com.Phys. Vietnam*, **30**, 85
 Homan W., Danilovich T., Decin L., de Koter A., Nuth J., Van de Sande M., 2018, *A&A*, **614**, A113
 Karovicova I., Wittkowski M., Ohnaka K., Boboltz D. A., Fossat E., Scholz M., 2013, *A&A*, **560**, A75
 Khouri T., et al., 2016, *A&A*, **591**, A70
 Khouri T., Velilla-Prieto L., De Beck E., Vlemmings W. H. T., Olofsson H., Lankhaar B., Black J. H., Baudry A., 2019, *A&A*, **623**, L1
 Knapp G. R., Pourbaix D., Platais I., Jorissen A., 2003, *A&A*, **403**, 993
 Lebzelter T., 1999, *A&A*, **351**, 644
 Maercker M., Danilovich T., Olofsson H., De Beck E., Justtanont K., Lombaert R., Royer P., 2016, *A&A*, **591**, A44
 Nhung P. T., Hoai D. T., Tuan-Anh P., Darriulat P., Diep P. N., Phuong N. T., Thai T. T., 2019, *MNRAS*, **490**, 3329
 Norris B. R. M., et al., 2012, *Nature*, **484**, 220
 Nowotny W., Höfner S., Aringer B., 2010, *A&A*, **514**, A35
 Ramstedt S., Olofsson H., 2014, *A&A*, **566**, A145
 Schöier F. L., Olofsson H., Wong T., Lindqvist M., Kerschbaum F., 2004, *A&A*, **422**, 651
 Schöier F. L., Ramstedt S., Olofsson H., Lindqvist M., Biegging J. H., Marvel K. B., 2013, *A&A*, **550**, A78
 Takigawa A., Kamizuka T., Tachibana S., Yamamura I., 2017, *Science Advances*, **3**, ea02149
 Takigawa A., Kim T.-H., Igami Y., Umemoto T., Tsuchiyama A., Koike C., Matsuno J., Watanabe T., 2019, *ApJ*, **878**, L7
 Van de Sande M., Decin L., Lombaert R., Khouri T., de Koter A., Wyrowski F., De Nutte R., Homan W., 2018, *A&A*, **609**, A63
 Villaver E., Livio M., Mustill A. J., Siess L., 2014, *ApJ*, **794**, 3
 Vlemmings W. H. T., et al., 2018, *A&A*, **613**, L4
 Vlemmings W. H. T., Khouri T., Olofsson H., 2019, *A&A*, **626**, A81
 Woitke P., 2006, *A&A*, **460**, L9
 Wong K. T., Kamiński T., Menten K. M., Wyrowski F., 2016, *A&A*, **590**, A127

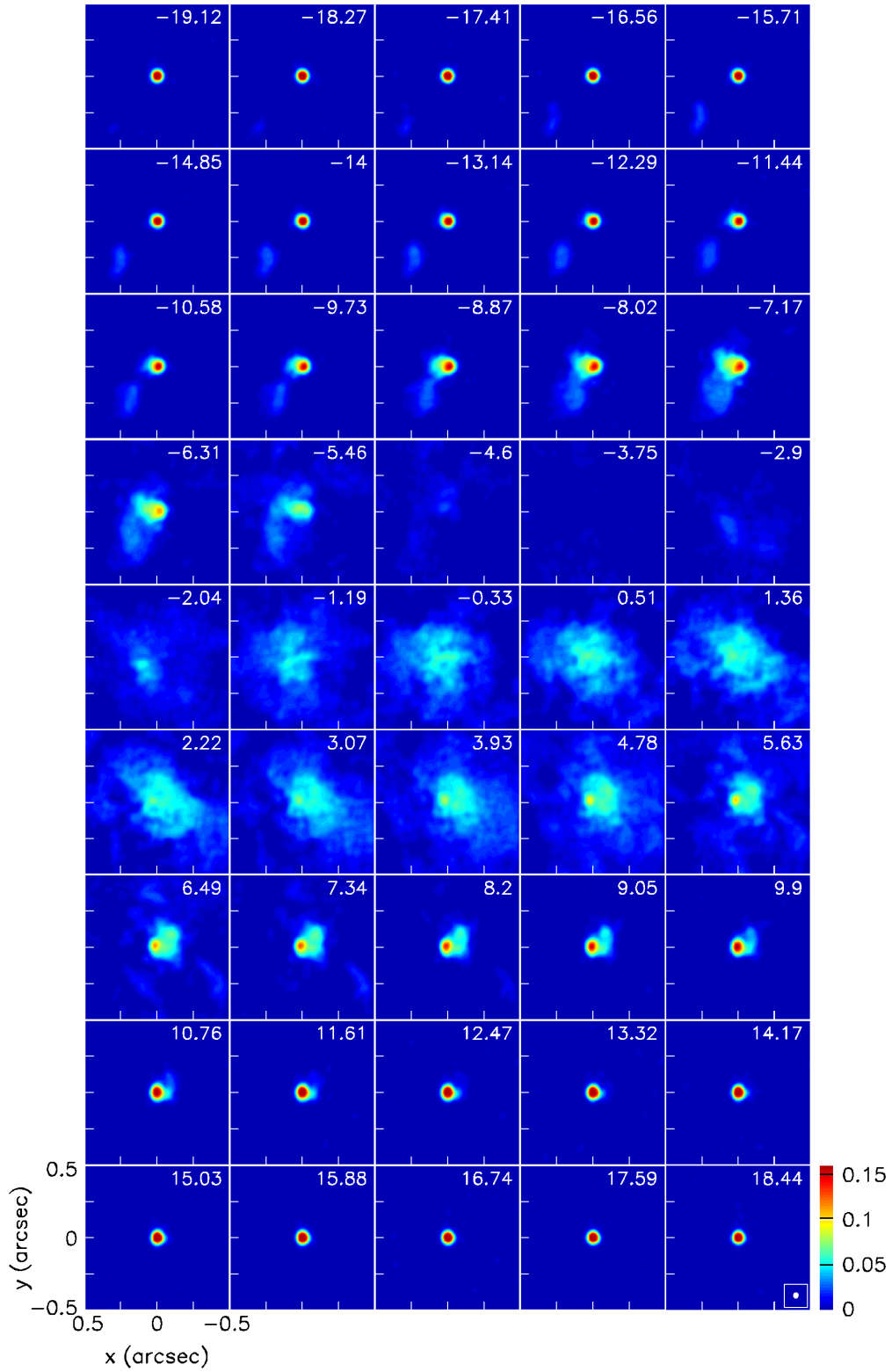


Figure A1. Channel map of ^{29}SiO emission (linear colour scale). The colour scale is in units of Jy beam^{-1} . The beam is shown in the lower-right corner of the last panel.

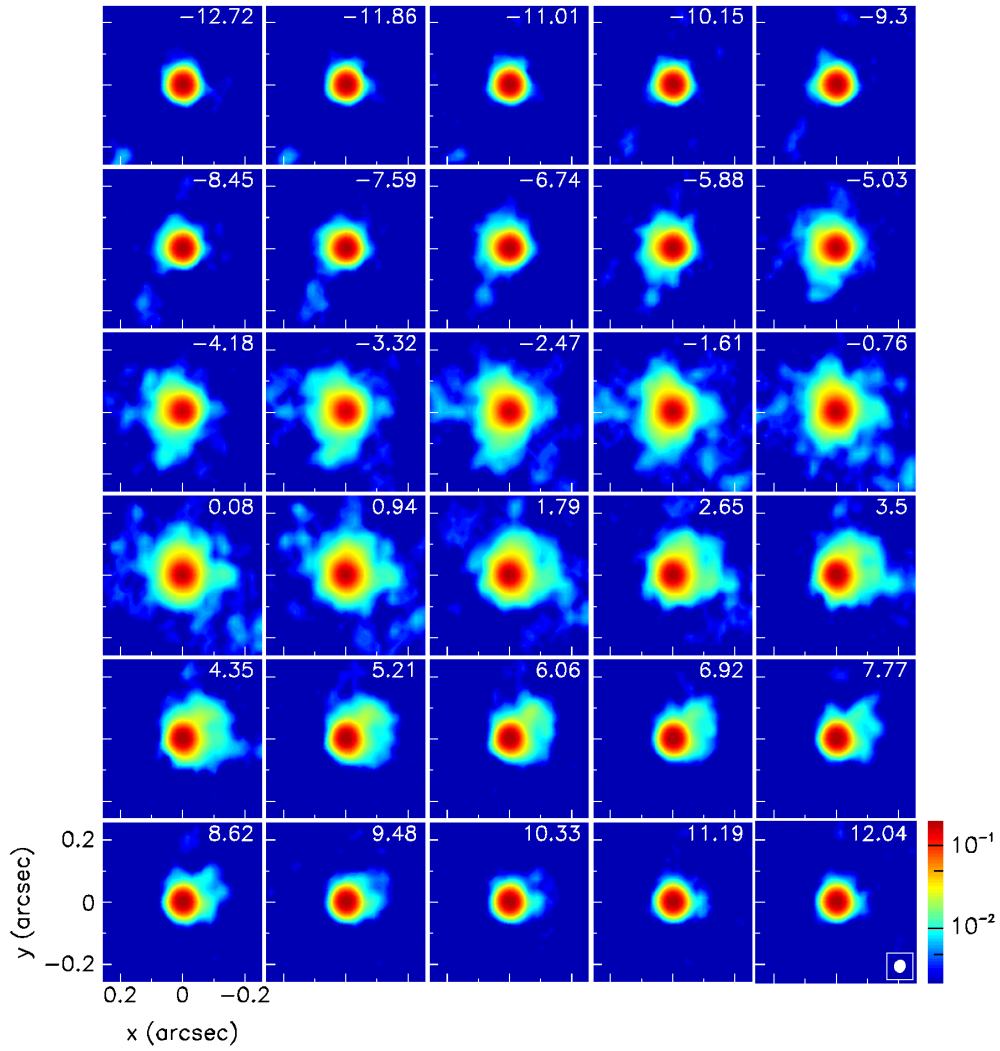


Figure A2. Channel map of SO₂ emission (log colour scale). The colour scale is in units of Jy beam⁻¹. The beam is shown in the lower-right corner of the last panel.

APPENDIX A:

This paper has been typeset from a $\text{\TeX}/\text{\LaTeX}$ file prepared by the author.

Table A1. Parameters of the best fits to the Doppler velocity distributions displayed in Figure 7.

SiO					
ring	quadrant	I^* (mJy)	I_0 (mJy)	V_{z0} (km s ⁻¹)	σ_0 (km s ⁻¹)
2	N	28	159	0.2	7.6
2	E	14	266	-3.1	5.4
2	S	13	171	0	6.6
2	W	19	190	3.5	7.5
3	N	8	292	1.1	5.1
3	E	-4	453	-3.0	4.1
3	S	-6	278	-0.7	4.6
3	W	9	325	4.4	4.1
4	N	-1	351	1.1	5.0
4	E	-4	461	-2.6	3.8
4	S	-3	318	-0.5	4.4
4	W	8	367	3.3	3.1
2	NE	21	220	-2.5	6.2
2	SE	14	205	-1.7	5.8
2	SW	15	172	2.8	7.2
2	NW	25	164	2.2	7.3
3	NE	-2	362	-2.1	4.7
3	SE	-1	368	-2.4	4.1
3	SW	4	259	2.6	4.2
3	NW	8	328	4.0	4.3
4	NE	-7	384	-1.3	4.5
4	SE	-3	418	-2.4	3.9
4	SW	3	339	2.6	2.9
4	NW	10	362	3.4	3.7

Table A2. Parameters of the best fits to the Doppler velocity distributions displayed in Figure 8.

SO ₂					
ring	quadrant	I^* (mJy)	I_0 (mJy)	V_{z0} (km s ⁻¹)	σ_0 (km s ⁻¹)
2	N	31	74	0	4.0
2	E	12	73	-2.6	3.9
2	S	14	67	0.1	3.9
2	W	21	61	2.3	4.7
3	N	8	52	0.7	3.9
3	E	-3	44	-2.3	3.5
3	S	-4	46	-2.1	3.3
3	W	8	55	3.1	3.7
4	N	3	26	0.3	3.9
4	E	-3	35	-2.0	3.1
4	S	0	35	-2.2	3.1
4	W	3	39	1.6	3.1
2	NE	21	76	-1.8	3.8
2	SE	13	69	-1.6	3.8
2	SW	18	63	1.9	4.3
2	NW	26	65	1.5	4.4
3	NE	3	52	-1.7	3.3
3	SE	-1	48	-2.7	3.0
3	SW	2	40	1.0	3.8
3	NW	6	62	3.0	3.9
4	NE	-1	39	-1.5	2.6
4	SE	-1	33	-2.9	3.5
4	SW	2	37	0.3	3.0
4	NW	5	29	2.3	3.9